Theoretical background I

Woven fabric composite properties

The stiffness properties and thermal expansion coefficients of composites strongly depend on the fibre orientation. A widely applied modelling technique for predicting these thermo–elastic properties of laminates built from unidirectional plies is the Classical Laminate Theory (CLT). The CLT is applied to flat plies in laminates where the fibre distribution and arrangement is homogeneous at the ply level. Weaves do not have a homogeneous fibre distribution, their fibres are concentrated in yarns. Additionally, the yarns are undulated in the weave. Therefore, the CLT cannot be applied directly to find the thermo–elastic properties of composites built from woven fabric reinforced composite materials.

Here, a model is presented that accounts for the structure of the weave and the fibre re–arrangement resulting from forming. It extends the CLT to account for the inhomogeneous fibre distribution in the weave and the undulation of the yarns. The model predicts the stiffness properties and thermal expansion coefficients of flat laminates builtup from non–orthogonal woven fabric plies. The model is verified with tensile tests and thermal expansion measurements on non–orthogonal weaves. Two types of fabric weaves were verified, a plain weave and a 8H satin weave.

Review on thermo–elastic modelling

Several models have been developed to predict the in–plane thermo–elastic properties of various fabric weaves. In the early nineties, Ishikawa and Chou [9, 10] developed three one–dimensional models for various types of orthogonal woven fabric composites: the mosaic model, the crimp model, and the bridging model. At the same time, the two–dimensional model of Naik and Shembekar [19, 20] described the full geometry of plain weave fabric laminates. The model predicts the in–plane elastic properties, based on the Classical Laminate Theory [23] and assuming a mixed parallel–series arrangement of infinitesimal pieces. Based on this model,

Falzon and Herzberg [12] considered the effect of the laminate configuration on the strength and stiffness properties in 1996. Vandeurzen and Verpoest [27,28] developed a Microsoft Excel©application, TEXCOMP, that describes the three–dimensional geometry of various fabric weaves. Based on this geometry, they developed a model that predicts the three–dimensional elastic properties of fabric composites. At the end of the nineties, Akkerman and De Vries [1] developed a two–dimensional model for orthogonal fabric weaves. In 2000, Lamers *et al.* [17] extended this model predicting the thermo–elastic properties of non–orthogonal, or skewed, weaves. The model presented here is a refinement of this work by adapting the yarn shape, resulting in better predictions of the weave properties. Recently, Hofstee *et al.* [14] presented a similar CLT based model to predict the thermo–elastic properties of thermo–formed skewed plain weaves.

Methodology

The weave is built from yarns, which consist of several thousands of fibres. The yarns cross over and under each other in weave patterns, introducing a waviness, or undulation, in the yarns. Undulated yarns are not orientated in the plane of the composite, and thus contribute less to the planar stiffness of the composite than yarns which remain in the plane. A geometrical model describes the weave pattern and the resulting waviness.

The fibres and the resin are not homogeneously distributed in the weave. The fibres are concentrated in the yarns and the matrix material is located in and around the yarns, bonding the fibres and transferring load. As a result, the fibre volume fraction is inhomogeneously distributed in the weave. It is generally accepted that the fibre volume fraction significantly affects the properties of the composite material. It is thus important to distinguish the geometry of the yarns in the composite in order to find the thermo–elastic properties of the composite.

A so called *top–down–bottom–up* method is employed to predict the thermo–elastic properties of a fabric reinforced composite (see figure 4). The method consists of two parts: the geometrical sub–division of the composite, or geometrical analysis, and the subsequent rebuilding of the weave with its thermo–elastic properties, or thermo–elastic analysis. The geometrical analysis is performed first, then the thermo–elastic analysis. Four structural levels are distinguished in the *top–down–bottom–up* method: the macro, the meso, the mini and the micro level.

The macro level considers the complete laminate. The geometrical analysis distinguishes the individual plies in the composite. It accounts for the lay–up of the composite. This part of the analysis is treated in section . The thermo–elastic analysis at the macro level (section) utilises a CLT based homogenisation technique

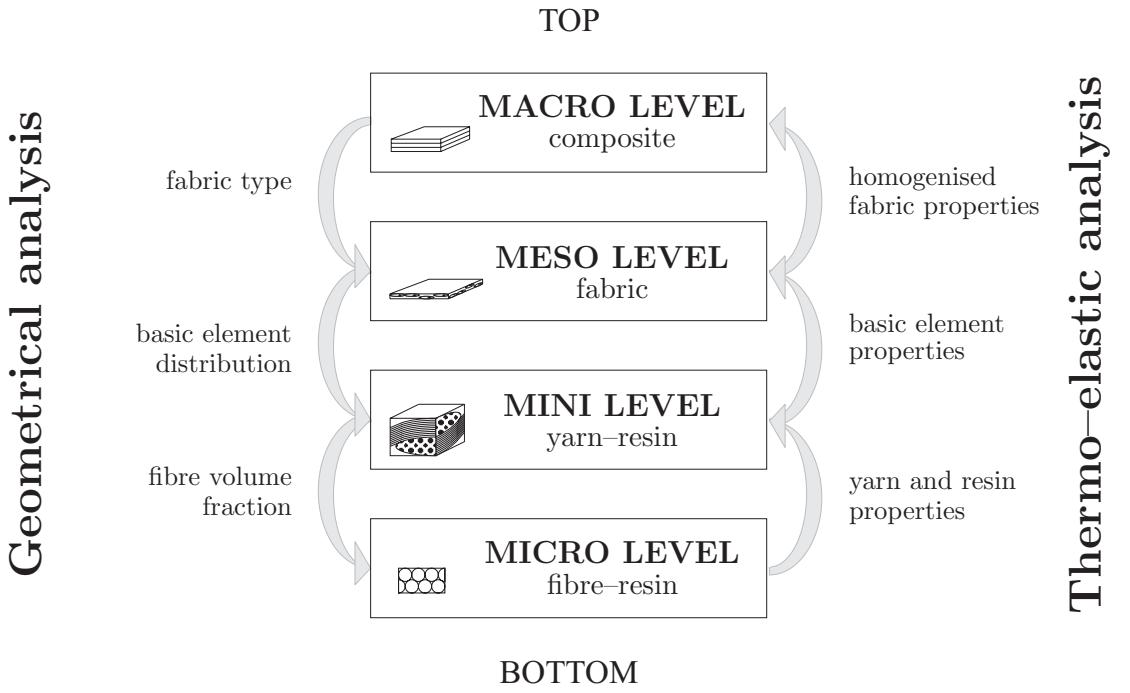

Figure 4: Top–down–bottom–up–method to predict the thermo–elastic properties of composites.

to determine the composite properties.

The meso level accounts for the weave architecture of the individual plies (section). Repetitive Volume Elements (RVE) are determined in the weave at this level. These RVE's are built from basic elements, the building block of any bi–axial weave. The thermo–elastic properties of the individual fabric layers are determined in section .

The mini level considers the basic elements of the weave. These building blocks distinguish the areas of resin and yarns and account for the undulation of the yarns. The geometrical description of the basic elements is covered in section . The thermo–elastic counterpart is treated in section .

Micromechanics are applied to obtain the homogenised properties of the yarns, combining the properties of fibres and resin at the micro level. The micro level geometrical analysis is considered in section while the thermo–elastic analysis is covered in section .

Geometrical analysis

The geometrical analysis, the *top-down* part of figure 4, considers the geometrical structure of the composite. The four levels, the macro, the meso, the mini and the micro level are treated in the following sections.

Macro level geometrical modelling

The composite is builtup from a number of plies. The lay–up, or stacking sequence, of these plies determines the structure of the composite. Symmetrical or non–symmetrical stacking sequences are distinguished at this level. The thickness, structure and orientation of the individual fabric layers are determined. Nesting of the individual plies is not taken into account; the fabric composite is considered as a flat ply with constant thickness.

Meso level geometrical modelling

The meso level considers the fabric ply and accounts for the weave architecture. The two yarn families, the warp and the fill yarns, are arranged into a specific order that identifies the weave pattern. RVE's can be distinguished at the meso level since the weave pattern is repetitive. These RVE's are the smallest regions that still can represent the weave, and are found in any two–dimensional weave.

The size of the RVE is determined by a specific number of warp and fill yarns for each weave pattern. Examples of a plain weave RVE and a satin RVE are depicted in figure 5.

The objective is to find building blocks within these RVE's. These building blocks, or basic elements (see section), model the weaves structure in order to distinguish areas of warp yarn, fill yarn and resin and account for the undulation in the yarns. Three RVE's for a plain weave are presented on the top part of figure 5. The plain weave RVE is 2 by 2 yarns and has four yarn crossings. Similarly, an RVE for an 8H satin weave is shown on the bottom half of the figure. It is 8 by 8 yarns.

Focusing on the plain weave RVE, it is observed that the fill yarn passes under and over the warp yarn respectively. The warp yarn passes over and under the fill yarn. Both yarn families are constantly undulated. Four yarn crossings occur in one plain weave RVE. Basic elements are used to represent these yarn crossings. Each crossing is represented by four basic elements.

The crossings in the plain weave can be modelled by one type of basic element, taking symmetry and anti–symmetry rules into account, as shown in figure 5. Both the warp and the fill yarn are undulated in this basic element. The name of the basic element type is A and is shown in black. Some of the A type basic elements

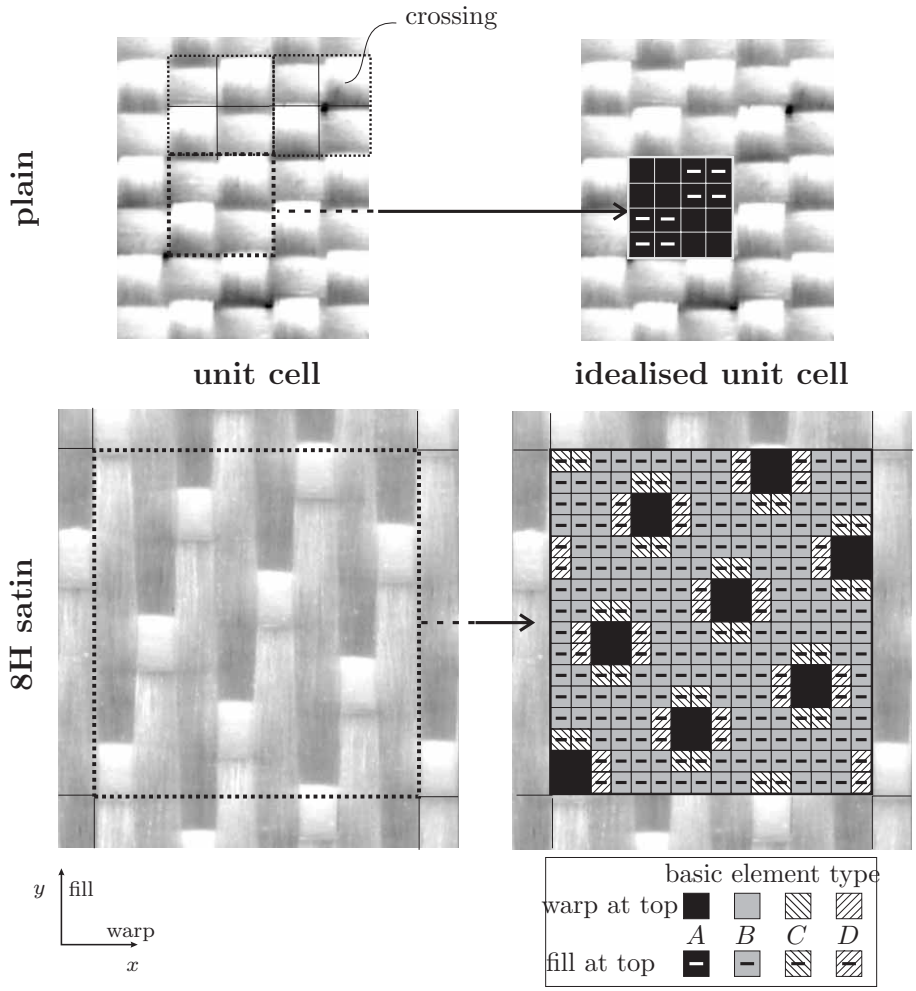

Figure 5: Repetitive Volume Element representation of a plain weave and an 8H satin glass weave by basic elements.

have a minus sign in figure 5, indicating that the fill yarns are on top. The plain weave RVE is modelled by 16 basic elements.

An example of an 8H satin RVE, marked with the dotted line, with most fill yarns on top is depicted in figure 5. Each fill yarn passes over seven warp yarns and then under one warp yarn in an 8H satin weave. Each warp yarn passes over seven fill and then under one fill yarn. The 8H satin RVE contains 64 crossings. Both the warp yarn and fill yarn are straight in most of these crossings.

The 8H satin RVE is composed of 256 basic elements. Four different types of basic elements can be distinguished: A, B, C and D. Both the warp and the fill yarn are

undulated in basic element A. Both the warp yarn and fill yarn are straight in basic element B. Basic elements C has a straight warp yarn and undulated fill yarn and basic element D has a straight fill yarn and an undulated warp yarn.

Each RVE of any bi–axially woven fabric can be described with these four different types of basic elements. The four basic element types and their yarn shape are listed in table 1.

Table 1: Basic elements and their yarn shape

Basic element	**A**	**B**	**C**	**D**
Warp shape	undulated	straight	straight	undulated
Fill shape	undulated	straight	undulated	straight

The structure of the basic elements is modelled at the mini level in the next section.

Mini level geometrical modelling

Regions of warp yarns, fill yarns and pure resin can be distinguished in the fabric composite. The basic elements represent the geometry of the fabric, as shown in section . The regions of warp yarn, fill yarn and resin are bounded by the yarn surfaces. These yarn surfaces are represented by geometrical shape functions for each of these basic elements, similar to the work of Naik and Shembekar [19, 20].

The yarn shape functions are defined by the yarn cross–sectional shape functions and the yarn mid–line functions. First the cross–sectional shape functions of the yarns are described, then the mid–line yarn functions. Finally, the description of the yarn surfaces is presented.

Yarn cross–sectional shape

The cross–section of the yarns are approximated with an ellipsoidal shape, possibly with a straight mid–section. The yarn cross–section is assumed to be constant along the yarn axis. The thickness or height of the yarn is assumed to be half of the thickness of the dry fabric, *i.e.* both fibre families have the same height in the current implementation. The longitudinal axis of the warp yarn is in the direction of the x–axis and the fill yarn is perpendicular to the warp yarn. A schematic representation of warp yarn cross–sectional shape in the yz–plane is given in figure 6.

In figure 6, the length of the yarn is denoted with l_y, the height with $\frac{1}{2}h_f$ and the yarn's straight part with l_{fy}. The function $s(y)$ describes the contour of the

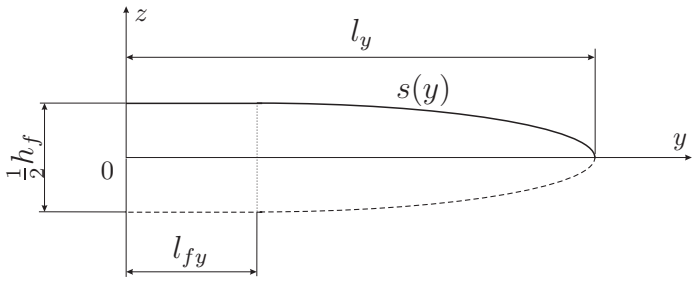

Figure 6: Cross–sectional shape of the warp yarn in the yz–plane.

right–top quarter of the yarn's cross–section. It consists of a straight part and a undulated part.

The length of the straight part is defined using an undulation factor. The undulation factor U_y relates the length of the straight part in the yarn's cross–section to the length l_y by:

$$l_{fy} = (1 - U_y)l_y. \tag{3}$$

The mathematical representations of $s(y)$, while accounting for the undulation, reads:

$$s(y) = \begin{cases} \frac{1}{4}h_f & \text{if} \quad 0 \leq y < l_{fy} \\ \frac{1}{4}h_f\sqrt{\left(1 - \frac{(y - l_{fy})^2}{{l_y}^2{U_y}^2}\right)} & \text{if} \quad l_y \geq y \geq l_{fy} \end{cases} \tag{4}$$

The entire contour of the warp yarn's cross–section is determined by combining the symmetric and anti–symmetric parts of $s(y)$. Similarly, a cross–section can be defined for the fill yarns in the xz–plane. It reads:

$$s(x) = \begin{cases} \frac{1}{4}h_f & \text{if} \quad 0 \leq x < l_{fx} \\ \frac{1}{4}h_f\sqrt{\left(1 - \frac{(x - l_{fx})^2}{{l_x}^2{U_x}^2}\right)} & \text{if} \quad l_x \geq x \geq l_{fx} \end{cases}, \tag{5}$$

where U_x is the undulation factor, l_x is the length in the cross–section of the fill yarn and l_{fx} is the length of the straight part in the cross–section of the fill yarn.

Yarn mid–line shape

The yarn families pass under and over each other in the fabric, resulting in undulation of the yarn families in their longitudinal direction. The height coordinate of the centre of the cross–section from the yarn thus changes in its longitudinal direction, as shown in figure 7.

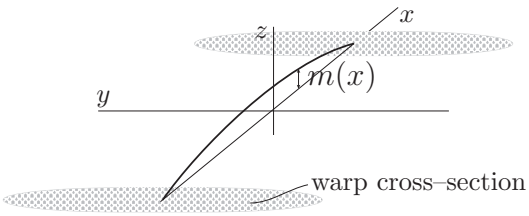

Figure 7: The warp yarn mid–line path. The fill yarn is not sketched for the propose of clarity.

Yarn contact is assumed at the crossings of the two fibre families. The shape of the mid–line path thus follows the cross–section of the other fibre family since the yarns do not penetrate or separate. Three parts define the mid–line path: I the straight part where the yarns are in contact; II the undulated part where the yarns are in contact; III a straight part where the yarns are not in contact. A schematic representation of the mid–line path function $m(x)$ of the warp yarn is presented in figure 8.

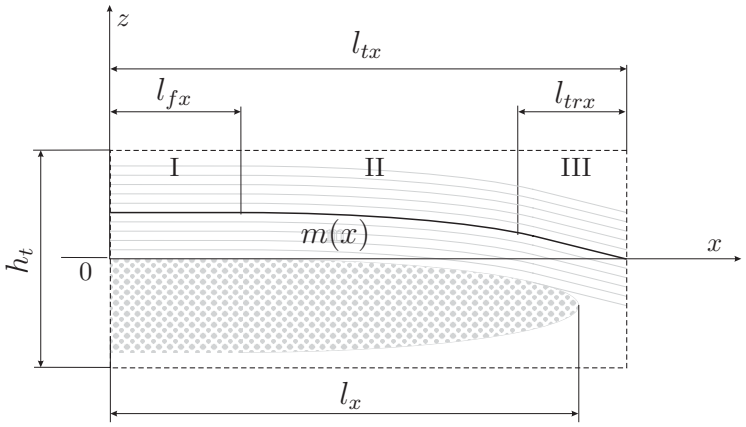

Figure 8: Mid–line path of the warp yarn in the xz–plane. The zones define the yarn mid–line.

In figure 8, h_t is the total thickness of the ply, l_{tx} is the length of the basic element in the x–direction and l_{trx} is the length of the straight part if the yarns are not in

contact. The three parts of the mid–line function $m(x)$ are described by:

$$m(x) = \begin{cases} m_I(x) = \frac{1}{4}h_f & \text{if} \quad 0 \le x < l_{fx} \\ m_{II}(x) = \frac{1}{4}h_f \sqrt{\left(1 - \frac{(x - l_{fx})^2}{{l_x}^2 {U_x}^2}\right)} & \text{if} \quad (l_{tx} - l_{trx}) > x \ge l_{fx} \\ m_{III}(x) = \frac{1}{4}h_f \frac{x - l_{tx}}{\sqrt{(l_{tx} - l_{fx})^2 - (l_f - l_{fx})^2}} & \text{if} \quad l_{tx} \ge x \ge (l_{tx} - l_{trx}) \end{cases} \tag{6}$$

The subfunction $m_{III}(x)$ in zone III, the straight part where the yarns are not in contact, is derived by solving the length of the straight part l_{trx}. The mid–line function $m(x)$ is required to be smooth and continuous over the full length, so the length l_{trx} is determined by applying a second order continuity condition at $x = l_{tx} - l_{trx}$:

$$m_{II}(x = l_{tx} - l_{trx}) = m_{III}(x = l_{tx} - l_{trx}); \tag{7}$$

$$\left.\frac{\partial m_{II}(x)}{\partial x}\right|_{x = l_{tx} - l_{trx}} = \left.\frac{\partial m_{III}(x)}{\partial x}\right|_{x = l_{tx} - l_{trx}}. \tag{8}$$

The length l_{trx} follows from solving (8), it reads:

$$l_{trx} = \frac{(l_{tx} - l_{lfx})^2 - (l_{fx} - l_{lfx})^2}{l_{tx} - l_{lfx}}. \tag{9}$$

The length l_{tx} of the basic element in the x–direction follows from the number of yarns per unit of length in the weave. The length is defined by :

$$l_{tx} = \frac{1}{2c_x}, \tag{10}$$

where c_x is the number of fill yarn per unit of length, or fill count. Again, the complete mid–line of the yarn can be described by combining symmetric and anti–symmetric variants of $m(x)$. Similarly, the mid–line function $m(y)$ of the fill yarn in the yz–plane is derived, it reads:

$$m(y) = \begin{cases} m_I(y) = \frac{1}{4}h_f & \text{if} \quad 0 \le y < l_{fy} \\ m_I(y) = \frac{1}{4}h_f \sqrt{\left(1 - \frac{(y - l_{fy})^2}{{l_y}^2 {U_y}^2}\right)} & \text{if} \quad (l_{ty} - l_{try}) > y \ge l_{fy} \\ m_I(y) = \frac{1}{4}h_f \frac{y - l_{ty}}{\sqrt{(l_{ty} - l_{fy})^2 - (l_f - l_{fy})^2}} & \text{if} \quad l_{ty} \ge y \ge (l_{ty} - l_{try}) \end{cases}, \tag{11}$$

where l_{ty} is the length of the basic element in the y–direction and l_{try} is the length of the straight part if the yarns are not in contact. The length l_{try} is derived similarly to the length l_{trx}. It reads:

$$l_{try} = \frac{(l_{ty} - l_{lfy})^2 - (l_{fy} - l_{lfy})^2}{l_{ty} - l_{lfy}}. \tag{12}$$

The length of the basic element in the y-direction is calculated from:

$$l_{ty} = \frac{1}{2c_y}, \tag{13}$$

where c_y is the warp count.

The basic elements A, B, C and D have straight and/or undulated yarns, as shown in table 1. The mid–line path functions of each of the basic elements define wether the yarn is undulated or straight. Setting $U_{x,y}$ to zero results in straight yarn paths in basic elements B, C and D.

Yarn surface functions

The yarn surface functions define the interfaces between regions of pure resin and yarns in the basic elements. The height position of the yarn surface h is created by a summation of the yarn mid–plane function m and the cross–sectional yarn shape functions s. The yarn mid–plane functions and the yarn shape functions are defined in perpendicular planes. The warp yarns are defined in the x–direction, the fill yarns are defined in the y–direction. The surfaces of the two fibre families are defined by:

$$\begin{aligned} h_T^{We}(x,y) &= m^e(x) + s(y) \\ h_B^{We}(x,y) &= m^e(x) - s(y) \\ h_T^{Fe}(x,y) &= -m^e(y) + s(x) \\ h_B^{Fe}(x,y) &= -m^e(y) - s(x) \end{aligned}, \tag{14}$$

where $h_T^{We}(x,y)$ and $h_B^{We}(x,y)$ define the warp top and bottom and $h_T^{Fe}(x,y)$ and $h_B^{Fe}(x,y)$ define the fill top and bottom interface for basic element e. Six surfaces define all interfaces when also defining the top and bottom plane. Combining symmetric and anti–symmetric basic elements describes the RVE. The graphical representation of the basic elements using the geometrical shape functions is displayed in figure 9.

The yarn height is constant in the xy–plane with the given shape functions (14). Therefore, the thickness in the undulated part differs from the thickness in the straight part of the yarn, as depicted in figure 10.
The yarn thickness is constant over its length. However, this second order deviation has no major effect on the resulting properties when the undulation angles remain smaller than 20° [12].

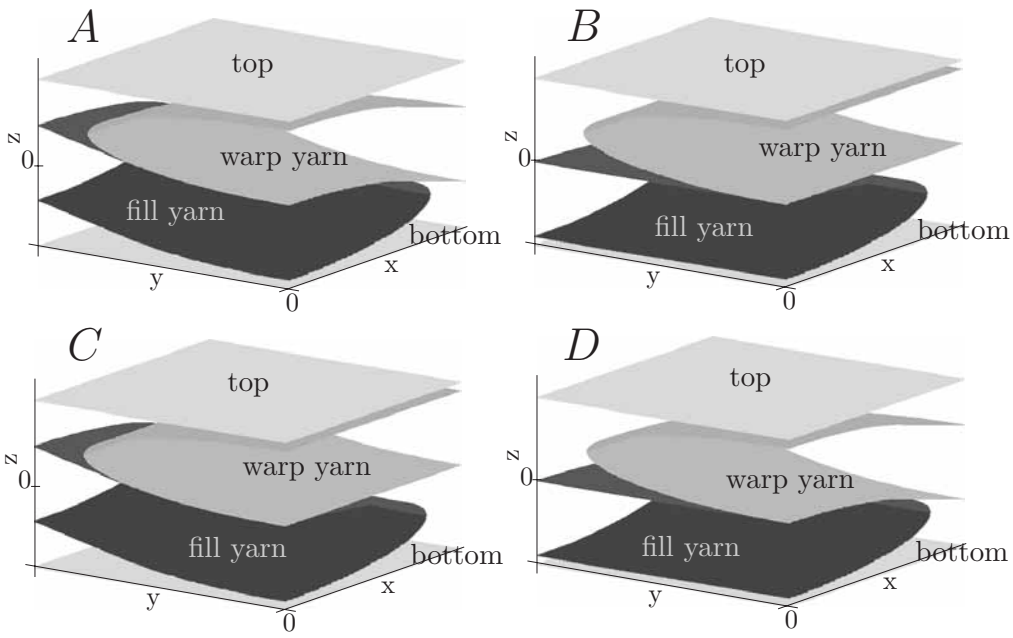

Figure 9: Basic elements A, B, C and D.

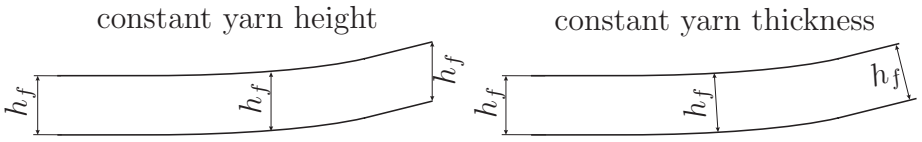

Figure 10: Yarn modelled with constant yarn height and constant yarn thickness.

Ply thickness

The undulation of the yarns depends on the thickness of the composite ply. The thickness of each fabric ply is determined by:

$$h_t = \frac{\rho_w}{V_f^C \rho_f}, \tag{15}$$

where V_f^C the composite fibre volume fraction and ρ_f the fibre density. ρ_w is the areal density of the weave, which is usually supplied by the manufacturer.

Yarn fibre volume fraction

The yarn fibre volume fraction is required to determine the thermo–elastic properties of the yarns. The size of the warp yarn, fill yarn and matrix regions determines the

average fibre volume fraction in the yarn regions. Micromechanical models are used to predict the material properties in the principal directions of the yarn (see section).

The shape functions define the regions with pure matrix material and regions with impregnated yarns (figure 9). The fibre volume fraction in the fibre bundles can be determined from geometrical considerations. The yarn fibre volume fraction, V_f^Y, can be related to the overall fibre volume fraction of the composite, by:

$$V_f^Y = \frac{\Omega^O}{\Omega^Y} V_f^C, \tag{16}$$

with Ω^O as the overall or total volume of the basic element and Ω^Y as the yarn volume. The superscript Y represents either the warp or fill yarn.

Shear transformation

The fabric is neither orthogonal nor uniformly deformed in many applications. Shear deformations of the weave beyond 30° are not uncommon during the production of composite products. The thermo–elastic properties need to be defined as a function of the skew angle for the prediction of shrinkage and warpage. Skewed means a shear deformation of the weave in this context, where the cross–over points in the weave act as pivoting points. The skew angle equals the material shear angle θ. The deformation is not pure shear since the thickness of the weave increases during shearing.

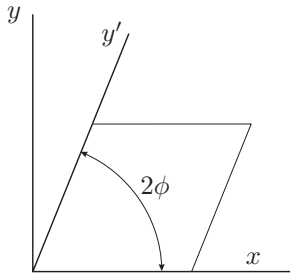

Figure 11: Shear transformation.

A transformation of the geometry is applied to incorporate the skew deformation, transforming the orthogonal axes into skewed axes, as depicted in figure 11, or mathematically described by:

$$\left\{ \begin{array}{c} x' \\ y' \end{array} \right\} = \left[\begin{array}{cc} 1 & 0 \\ \cos 2\phi & \sin 2\phi \end{array} \right] \cdot \left\{ \begin{array}{c} x \\ y \end{array} \right\} \tag{17}$$

where x' and y' are the transformed axes and 2ϕ the enclosed fibre angle. The area of the RVE decreases with increasing skew angle as a result of this in–plane transformation. It was observed in the picture frame experiments (chapter **??**) that the composite thickness increases during shear deformation, while the volume remained constant. The thickness of the fabric in deformed axes is related to the initial thickness by:

$$h(x', y') = \frac{h(x, y)}{\cos(2\phi_o - 2\phi)}, \tag{18}$$

where $h(x, y)$ is the thickness of the ply corresponding to the initial fabric angle $2\phi_o$.

Micro level geometrical modelling

The micro level geometrical modelling considers the microstructure of the yarns. Each yarn usually contains of several thousand fibres and resin. The fibres in the yarns are arranged along the yarn axis. Packing models idealise the arrangement of the fibres in the yarns. Generally two fibre idealisation models are considered: the square and the hexagonal packing. The square and hexagonal packing structures are depicted in figure 12.

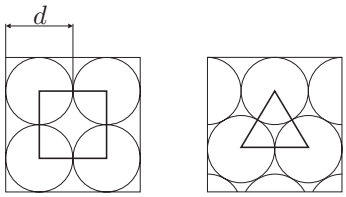

Figure 12: Square and hexagonal packing of fibres.

The packing structure also determines the theoretical maximum fibre volume fraction when assuming circular fibre cross–sections. When the fibres have a diameter d the maximum volume fraction for the square packing is:

$$V_f = \frac{\frac{1}{4}\pi d^2}{d^2} = \frac{\pi}{4} \approx 0.785. \tag{19}$$

The maximum fibre volume fraction for the hexagonal packing is:

$$V_f = \frac{\frac{1}{8}\pi d^2}{\frac{1}{4}\sqrt{3}d^2} = \frac{\pi}{2\sqrt{3}} \approx 0.907. \tag{20}$$

The maximum fibre volume fraction in the square packing is 13% lower than the maximum fibre volume fraction in the hexagonal packing.

Thermo–elastic analysis

The mechanical analysis, the *bottom–up* part in figure 4, considers the thermo–elastic properties of the composite. The four levels: micro, mini, meso and macro level are treated in the following sections.

Micro level thermo–elastic modelling

Mechanical modelling at the micro level considers the thermo–elastic properties of the yarns and the resin. The resin is assumed isotropic, and its thermo–elastic properties are therefore straightforward to derive. The properties of the yarns are derived by micromechanical modelling.

Micromechanical models predict the elastic properties and the thermal expansion coefficients of UD materials. The micromechanical models account for anisotropy in the constituents, the composition and the internal microstructure (fibre size, shape, and packing geometry) to predict the macroscopic properties of the UD material.

Two types of predictions will be examined: models that predict the elastic properties and models that predict the linear thermal expansion coefficients. An extensive survey on these model was published by Whitney and McCullough [29]. However, splitting the models into two types does not imply that the models are based on a different theoretical approach. The predictions from, for example, the rule–of–mixtures models for elastic properties are based on exactly the same approach as the rule–of–mixtures models for the prediction of the linear thermal expansion coefficients.

Elastic properties models

The use of the simple iso–stress and iso–strain models as the rule–of–mixtures models [29] is widely applied, although they are known to underestimate the transverse properties of the composite. More advanced non–uniform stress or strain field energy based models such as the Composite Cylinder Assemblage (CCA) model by Hashin [13] or the Chamis models [8] are also used by several authors. The use of semi–empirical models, such as the Puck model [21] or Halpin–Tsai models [29], is also widely spread.

A micromechanical model was selected based on a UD composite study. An E–glass/epoxy composite with a fibre volume fraction of 55% was selected in order to perform this study. The material parameters of the constituents was obtained from literature [6, 22]. The measured values of the elastic and thermal properties of the composite are also obtained in the literature [11]. The best fitting models for the UD material were the rule–of–mixtures model in the longitudinal fibre direction and the Composite Cylinder Assemblage (CCA) model in the transverse to the fibre

direction. The results of the two models are combined to predict the UD properties in the longitudinal and transverse direction.

Coefficient of thermal expansion models

Similarly to the elastic properties models, many models to predict the thermal expansion are available in literature. Again, the simple iso–stress and iso–strain based rule–of–mixtures [29] models can be applied to find the linear thermal expansion coefficients of UD materials. Other models such as the Schapery model [25], the models proposed by Rosen and Hashin [24], the Chamberlain model [5], or the Schneider model [26] can also be found in literature.

The micromechanical models are selected based on a similar study as the elastic properties models in section . The rule–of–mixtures model fitted the literature data [11] best in the longitudinal fibre direction. The Schapery model approximated the transverse thermal expansion coefficients best. Two models are combined to predict the thermal expansion coefficients in the longitudinal and transverse direction.

Mini level thermo–elastic modelling

The thermo–elastic properties of the basic elements are calculated using the geometrical representation of the weave from section . The properties of the basic elements are subsequently used to determine the RVE thermo–elastic properties. First, the elastic properties of the basic elements are derived, then the thermal behaviour of the basic elements are determined.

Elastic properties

It is assumed that the CLT [23] is applicable to each of the basic elements. The CLT is based on the Kirchhoff plate theory, which assumes plane stress and zero transverse shear. The strain profile through–the–thickness $\{\varepsilon(z)\}$ of thin plates is given by:

$$\{\varepsilon(z)\} = \{\varepsilon^o\} + z\{\kappa\}, \tag{21}$$

where $\{\varepsilon^o\}$ and $\{\kappa\}$ are the mid–plane strain and curvature of the plate and z the height coordinate. The stress profile $\{\sigma(z)\}$ follows automatically by multiplying equation (21) with the elastic in–plane stiffness matrix $[Q(z)]$:

$$\{\sigma(z)\} = [Q(z)] \cdot \{\varepsilon(z)\}. \tag{22}$$

The load and moment vector N_i and M_i result from the integration of the stress

profile from equation 22 through–the–thickness, as:

$$\begin{aligned}
\{N\} &= \int_{h_B}^{h_T} \{\sigma(z)\}\, dz = \int_{h_B}^{h_T} [Q(z)] \cdot \{\varepsilon(z)\}\, dz \\
&= \int_{h_B}^{h_T} [Q(z)] \cdot (\{\varepsilon^o\} + z\{\kappa\})\, dz \\
\{M\} &= \int_{h_B}^{h_T} \{\sigma(z)\}\, z\, dz = \int_{h_B}^{h_T} [Q(z)] \cdot \{\varepsilon(z)\}\, z\, dz \\
&= \int_{h_B}^{h_T} [Q(z)] \cdot (z\{\varepsilon^o\} + z^2\{\kappa\})\, dz
\end{aligned} \quad , \tag{23}$$

where h_B is the bottom and h_T is the top coordinate of the ply. Writing equation 23 in matrix form results in:

$$\left\{ \begin{array}{c} N \\ M \end{array} \right\} = \int_{h_B}^{h_T} \left[\begin{array}{cc} Q(z) & Q(z)\, z \\ Q(z)\, z & Q(z)\, z^2 \end{array} \right] \cdot \left\{ \begin{array}{c} \varepsilon^o \\ \kappa \end{array} \right\} dz \tag{24}$$

As a result, the constitutive equation for the CLT based mechanical properties for a ply is:

$$\left\{ \begin{array}{c} N_i \\ M_i \end{array} \right\} = \left[\begin{array}{cc} A_{ij} & B_{ij} \\ B_{ij} & D_{ij} \end{array} \right] \left\{ \begin{array}{c} \varepsilon_j^o \\ \kappa_j \end{array} \right\}, \qquad \text{where } i, j = 1, 2 \text{ or } 6 \tag{25}$$

with

$$(A_{ij}, B_{ij}, D_{ij}) = \int_{h_B}^{h_T} Q_{ij}(z)\, (1, z, z^2)\, dz \tag{26}$$

in which h_B is the bottom coordinate, and h_T is the top coordinate of the ply.

$[Q(z)]$ is piecewise constant through–the–thickness for laminates builtup from unidirectional (UD) plies. Additionally, for UD plies, $[Q(z)]$ is independent of the in–plane coordinates x and y and the height coordinates of each ply remains constant. The integral from equation (26) can be solved straightforwardly.

Here, the boundaries for integration in equation (26) are determined by the yarn surface functions in the basic element. Additionally, the yarns are undulated. The homogenised properties of the warp yarn, fill yarn and resin were derived in section . As a result, $[Q(z)]$ is piecewise constant in the thickness direction for any position (x, y) in the basic element.

The warp yarns, fill yarns and resin each have an in–plane stiffness matrix. The resin is isotropically; the resin in–plane stiffness matrix $[Q^R]$ is constant over the basic element. The warp yarn and fill yarn are rotated in the plane and undulated in the basic element.

The in–plane stiffness matrix of the yarn $[Q^Y]$, where the suffix Y stands for warp or fill respectively, is defined in xyz–coordinates and obtained from an in–plane rotation of the $[\tilde{Q}^Y]$ stiffness matrix by [23]:

$$[Q^Y] = [T]^{-1} \cdot [\tilde{Q}^Y] \cdot [R] \cdot [T] \cdot [R]^{-1}, \tag{27}$$

where $[\tilde{Q}^Y]$ is defined in the ply 123–coordinates, which lie in the yarn directions. $[R]$ is the Reuter matrix and $[T]$ is the in–plane rotation matrix:

$$[T] = \begin{bmatrix} \cos^2\zeta & \sin^2\zeta & 2\sin\zeta\cos\zeta \\ \sin^2\zeta & \cos^2\zeta & -2\sin\zeta\cos\zeta \\ -\sin\zeta\cos\zeta & \sin\zeta\cos\zeta & \cos^2\zeta - \sin^2\zeta \end{bmatrix}, \tag{28}$$

where the angle ζ is defined by the in–plane orientation of the yarn to the xyz–coordinates. $[\tilde{Q}^Y]$ is derived from the in–plane elastic constants of each ply with undulated yarns as:

$$[\tilde{Q}^Y] = \begin{bmatrix} Q_{11} & Q_{12} & 0 \\ Q_{21} & Q_{22} & 0 \\ 0 & 0 & Q_{66} \end{bmatrix} = \begin{bmatrix} \frac{E_1}{1-\nu_{12}\nu_{21}} & \frac{\nu_{12}E_2}{1-\nu_{12}\nu_{21}} & 0 \\ \frac{\nu_{21}E_1}{1-\nu_{12}\nu_{21}} & \frac{E_2}{1-\nu_{12}\nu_{21}} & 0 \\ 0 & 0 & G_{12} \end{bmatrix}, \tag{29}$$

Here, E is the modulus, G is the shear modulus and ν is the Poisson's ratio.

However, the yarns are undulated in the basic elements. The in–plane elastic contribution of the yarns are a function of the local yarn angle ϱ in each basic element e, which is the first derivative of the yarn mid–line functions:

$$\begin{aligned} \varrho(x)^e &= \arctan\left(\frac{\partial m(x)^e}{\partial x}\right) \\ \varrho(y)^e &= \arctan\left(\frac{\partial m(y)^e}{\partial y}\right) \end{aligned}. \tag{30}$$

The effective in–plane elastic constants of the warp and fill yarns can be described using the undulation angles $\varrho(x)^e$ and $\varrho(y)^e$ of these yarns as [12]:

$$\begin{aligned} E_1(\varrho) &= \left[\frac{\cos^4\varrho}{E_l} + (\frac{1}{G_{lt}} - \frac{2\nu_{lt}}{E_l})\cos^2\varrho\sin^2\varrho + \frac{\sin^4\varrho}{E_t}\right]^{-1} \\ E_2(\varrho) &= E_t \\ \nu_{12}(\varrho) &= E_1(\varrho)\left[\frac{\cos^2\varrho\,\nu_{lt}}{E_l} + \frac{\sin^2\varrho\,\nu_{tt}}{E_t}\right] \\ G_{12}(\varrho) &= \left[\frac{\cos^2\varrho}{G_{lt}} + \frac{\sin^2\varrho}{G_{tt}}\right]^{-1} \end{aligned}, \tag{31}$$

Here, the suffix l and t represent longitudinal and transverse direction respectively.

Accounting for the boundaries of the shape functions, substituting these into equation (26), and subsequent integration for each of the areas, results in:

$$\begin{aligned} A^e_{ij}(x,y) &= Q^R_{ij}\left[h_T^{We}(x,y) - h_T(x,y) + h_B(x,y) - h_B^{Fe}(x,y)\right] + \\ &\quad Q^W_{ij}(\varrho(x)^e)\left[h_B^{We}(x,y) - h_T^{We}(x,y)\right] + \\ &\quad Q^F_{ij}(\varrho(y)^e)\left[h_B^{Fe}(x,y) - h_T^{Fe}(x,y)\right] \qquad (32a) \\ B^e_{ij}(x,y) &= \tfrac{1}{2}Q^R_{ij}\left[h_T^{We}(x,y)^2 - h_T(x,y)^2 + h_B(x,y)^2 - h_B^{Fe}(x,y)^2\right] + \\ &\quad \tfrac{1}{2}Q^W_{ij}(\varrho(x)^e)\left[h_B^{We}(x,y)^2 - h_T^{We}(x,y)^2\right] + \\ &\quad \tfrac{1}{2}Q^F_{ij}(\varrho(y)^e)\left[h_B^{Fe}(x,y)^2 - h_T^{Fe}(x,y)^2\right] \qquad (32b) \\ D^e_{ij}(x,y) &= \tfrac{1}{3}Q^R_{ij}\left[h_T^{We}(x,y)^3 - h_T(x,y)^3 + h_B(x,y)^3 - h_B^{Fe}(x,y)^3\right] + \\ &\quad \tfrac{1}{3}Q^W_{ij}(\varrho(x)^e)\left[h_B^{We}(x,y)^3 - h_T^{We}(x,y)^3\right] + \\ &\quad \tfrac{1}{3}Q^F_{ij}(\varrho(y)^e)\left[h_B^{Fe}(x,y)^3 - h_T^{Fe}(x,y)^3\right], \qquad (32c) \end{aligned}$$

where the subscript R, W and F denote resin, warp and fill, respectively, and superscript e denotes the type of basic element (A, B, C or D). $[Q^R]$ is derived by substituting the resin modulus, Poisson's ratio and shear modulus into 29.

The average CLT stiffness matrices for each basic element can now be obtained using the two–dimensional woven fabric model [19, 20]. The model can predict an upper and lower boundary for the CLT stiffness matrices by assuming in–plane iso–strain or iso–stress conditions, respectively called the *Parallel-Parallel* (PP) and the *Series-Series* (SS). The upper boundary is predicted by:

$$\left(\overline{A}^{e,PP}_{ij}, \overline{B}^{e,PP}_{ij}, \overline{D}^{e,PP}_{ij}\right) = \frac{1}{l^W_t l^F_t}\int_0^{l^F_t}\int_0^{l^W_t}\left(A^e_{ij},\, B^e_{ij},\, D^e_{ij}\right) dxdy \qquad (33)$$

The $[abhd]^{e,PP}$ compliance matrix can be obtained by substituting $[\overline{A}]^{e,PP}$, $[\overline{B}]^{e,PP}$ and $[\overline{D}]^{e,PP}$ in the CLT constitutive equation (25) and inverting the resulting $[ABD]^{e,PP}$ stiffness matrix. $[h]$ equals $[b]^T$ in the $[abhd]$ matrix. The lower boundary for the stiffness is obtained via the compliance matrix form:

$$\left(\overline{a}^{e,SS}_{ij}, \overline{b}^{e,SS}_{ij}, \overline{d}^{e,SS}_{ij}\right) = \frac{1}{l^W_t l^F_t}\int_0^{l^F_t}\int_0^{l^W_t}\left(a^e_{ij},\, b^e_{ij},\, d^e_{ij}\right) dxdy. \qquad (34)$$

The $[ABD]^{e,SS}$ stiffness matrix is obtained by inverting $[abhd]^{e,SS}$. The integrals from equations 33 and 34 are evaluated numerically using Gauss–Legendre quadrature [3].

Thermal properties

The thermal properties of the basic elements are determined under the same assumptions as the mechanical properties of the basic elements. The equations for the thermal forces then become:

$$\left\{ \begin{array}{c} \tilde{N}_i^e \\ \tilde{M}_i^e \end{array} \right\} = -\Delta T \left\{ \begin{array}{c} \overline{N}_i^e \\ \overline{M}_i^e \end{array} \right\}, \tag{35}$$

in which

$$\overline{N}_i^e = \int_{h_B}^{h_T} q_i^e(x,y)\, dz, \qquad \overline{M}_i^e = \int_{h_B}^{h_T} q_i^e(x,y)\, z\, dz, \tag{36}$$

and

$$q(x,y)_i^e = Q_{ij}^e(x,y)\, \alpha_j(x,y). \tag{37}$$

Here, $\{\alpha(x,y)\}$ contains the thermal expansion coefficients with respect to the xyz–coordinate system of the warp or fill yarn or the matrix material. $\{\alpha(x,y)\}$ is obtained by in–plane rotation of $\{\alpha^{123}\}$, similarly to the rotation of the in–plane stiffness matrix, it reads:

$$\{\alpha(x,y)\} = [R] \cdot [T]^{-1} \cdot [R]^{-1} \{\alpha^{123}\}, \tag{38}$$

where

$$\begin{array}{l} \alpha_1^{123} = \alpha_l \cos^2 \varrho + \alpha_t \sin^2 \varrho \\ \alpha_2^{123} = \alpha_t \qquad\qquad\qquad\qquad , \\ \alpha_{12}^{123} = 0 \end{array} \tag{39}$$

where α_l and α_t are the thermal expansion coefficients in the longitudinal and transverse direction of the yarn respectively. The thermal expansion coefficients of the warp and fill yarn depend on the fibre volume fraction and are determined using the rule–of–mixtures model and the model of Schapery [25].

The thermally induced forces and moments are determined by substituting Q_{ij} by q_i in part a and b of equation (32) respectively. When assuming no external force the resulting thermal strain and curvature for the basic elements are:

$$\left\{ \begin{array}{c} \tilde{\varepsilon}^{o,e} \\ \tilde{\kappa}^e \end{array} \right\} = -\Delta T \left[\begin{array}{cc} \overline{a}^e & \overline{b}^e \\ \overline{h}^e & \overline{d}^e \end{array} \right] \cdot \left\{ \begin{array}{c} \overline{N}^e \\ \overline{M}^e \end{array} \right\}. \tag{40}$$

A lower and upper boundary can also be predicted for the thermal strain and curvature. They are determined by substituting the $[abhd]$ compliance matrix following from an iso–strain or iso–stress configuration into equation (40). The in–plane thermal strain and curvature coefficients per °C$\{\overline{\varepsilon}^o\}^e$ and $\{\overline{\kappa}\}^e$ are:

$$\left\{ \begin{array}{c} \overline{\varepsilon}^{o,e} \\ \overline{\kappa}^e \end{array} \right\} = \left[\begin{array}{cc} \overline{a}^e & \overline{b}^e \\ \overline{h}^e & \overline{d}^e \end{array} \right] \cdot \left\{ \begin{array}{c} \overline{N}^e \\ \overline{M}^e \end{array} \right\}. \tag{41}$$

Meso level thermo–elastic modelling

The unit cell properties are determined in the meso level using the basic elements properties of section . Two approaches are distinguished here, the averaging approach and the Finite Element (FE) approach.

Averaging approach

The thermo–elastic properties of the weave are determined by volume averaging of the properties of all basic elements in the RVE. A lower and an upper bound of the basic element properties were obtained, using an iso–strain and iso–stress configuration respectively. Similar assumptions can be applied for the averaging approach, resulting in four possible combinations. Two combinations are based on an iso–strain assumption in the RVE, the other two assume an iso–stress in the RVE. However, the assumption of iso–stress leads to an severe underestimation of the stiffness properties of the fabric weave and is therefore not used in this analysis.

All basic elements have an equal volume. As a result, the average thermo–elastic properties of the RVE are determined by:

$$\begin{aligned}
[A]^R &= \frac{1}{m_t}\left(m_a\overline{[A]}^a + m_b\overline{[A]}^b + m_c\overline{[A]}^c + m_d\overline{[A]}^d\right)\\
[B]^R &= \frac{1}{m_t}\left(m_a\overline{[B]}^a + m_b\overline{[B]}^b + m_c\overline{[B]}^c + m_d\overline{[B]}^d\right),\\
[D]^R &= \frac{1}{m_t}\left(m_a\overline{[D]}^a + m_b\overline{[D]}^b + m_c\overline{[D]}^c + m_d\overline{[D]}^d\right)
\end{aligned} \tag{42}$$

where m represents the number of basic elements. The subscript t indicates total and a, b, c and d stand for the type of basic element. The RVE's lower and upper stiffness bound can be determined by averaging the basic element PP or SS configuration, respectively.

The thermal loading vector is derived similarly to the CLT stiffness matrices. The volume averaged thermal loading vectors read:

$$\begin{aligned}
\{\tilde{N}\}^R &= \frac{1}{m_t}\left(m_a\{\tilde{N}\}^a + m_b\{\tilde{N}\}^b + m_c\{\tilde{N}\}^c + m_d\{\tilde{N}\}^d\right)\\
\{\tilde{M}\}^R &= \frac{1}{m_t}\left(m_a\{\tilde{M}\}^a + m_b\{\tilde{M}\}^b + m_c\{\tilde{M}\}^c + m_d\{\tilde{M}\}^d\right)
\end{aligned}. \tag{43}$$

Finite Elements approach

An FE approach can be used, alternatively to the averaging approach, leading to closer bounds for the unit cell stiffness.

Equations (21) and (22) are substituted in the equation of virtual work, containing the volume integral of the element stiffnesses and displacements and the surface integral of the applied forces:

$$\delta\Pi = \int\limits_A \int\limits_h \{\delta\varepsilon^o \ + z\delta\kappa\}^T \cdot \{[Q] \cdot \{\varepsilon^o \ + z\kappa\}\} dz dA - \int\limits_\Gamma \delta v \cdot t \, d\Gamma \equiv 0 \quad (\forall \delta\varepsilon, \delta\kappa), \tag{44}$$

Here, A is the area, h is the thickness, $\delta\varepsilon^o$ and $\delta\kappa$ are the virtual strains and curvatures, δv the virtual displacements and rotations, t the tractions and Γ is the boundary. The body forces are assumed to be zero. The FE representation then uses:

$$\begin{aligned} \{\delta\varepsilon^o\} = [B_m] \cdot \{\delta u\}, \quad \{\varepsilon^o\} = [B_m] \cdot \{u\} \\ \{\delta\kappa\} = [B_b] \cdot \{\delta\phi\}, \quad \{\kappa\} = [B_b] \cdot \{\varphi\} \end{aligned} \tag{45}$$

where B_m and B_b contain the first derivatives of the FE trial functions of, respectively, the element displacements, $\{u\}$, and rotations, $\{\varphi\}$. The virtual displacements and rotations are denoted by $\{\delta u\}$ and $\{\delta\varphi\}$, respectively. Thus, an FE formulation is found, symbolically written as:

$$\int\limits_A \begin{bmatrix} B_m & 0 \\ 0 & B_b \end{bmatrix}^T \cdot \begin{bmatrix} A & B \\ B^T & D \end{bmatrix} \cdot \begin{bmatrix} B_m & 0 \\ 0 & B_b \end{bmatrix} dA \cdot \begin{Bmatrix} u \\ \varphi \end{Bmatrix} = \{F\}, \tag{46}$$

where $\{F\}$ contains the prescribed nodal forces.

The Discrete Kirchhoff Triangle (DKT) element with three in–plane integration points is used to solve the FE problem [4, 7]. Each basic element is represented by four finite elements. The thermo–elastic basic element properties, derived in section , are used in each of the FE elements. The plain weave RVE is described with 4×4 basic elements, resulting in a mesh of 64 elements. The 8H satin weave is computationally less attractive. The RVE of an 8H satin weave is described with 16×16 of these quadrilaterals, resulting in a mesh of 1024 elements. The FE mesh for a basic element is depicted in figure 13.

Elementary loading conditions are applied to the FE mesh, resulting in deformations of the FE mesh. Six loading and corresponding deformation sets are required to filter the mechanical properties of the RVE. The RVE is based on periodicity in the weave. Therefore, periodicity must also be preserved in the deformed RVE. Constraint equations on the sides of the RVE are used to guarantee the periodicity.

To this end, a linear relation is prescribed between the difference in nodal displacements and rotations of the opposite RVE sides and the nodal displacements and rotations of the RVE corner nodes. The actual constraint equations can be explained using figure 14.

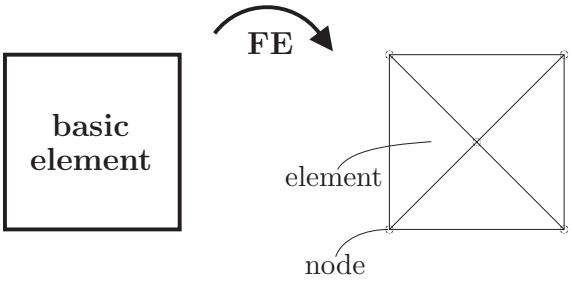

Figure 13: Representation of a basic element by four FE elements.

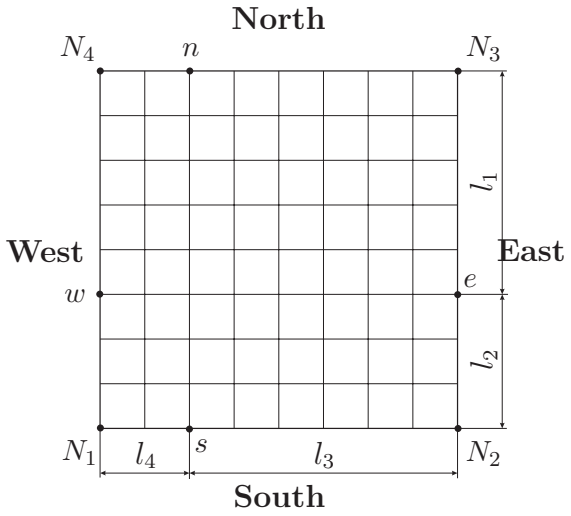

Figure 14: Constraints on the sides of the RVE.

All degrees of freedom U_e and U_w, *i.e.* all separate nodal displacements u and rotations φ, of two opposite nodes e and w at the east and west side respectively, of the RVE are constrained by:

$$\begin{aligned} U_e - U_w &= \frac{l_2}{l_1 + l_2}\Delta U_N - \frac{l_1}{l_1 + l_2}\Delta U_S \\ \Delta U_N &= U_4 - U_3 \\ \Delta U_S &= U_2 - U_1 \end{aligned} \tag{47}$$

in which the subscripts N, S, E and W refer to North, South, East and West, respectively. The subscript 1, 2, 3 and 4 indicate the corner nodes of the RVE. For

the north and south side the constraints are similar:

$$\begin{aligned} U_n - U_s &= \frac{l_4}{l_3 + l_4}\Delta U_E - \frac{l_3}{l_3 + l_4}\Delta U_W \\ \Delta U_E &= U_3 - U_2 \\ \Delta U_W &= U_4 - U_1 \end{aligned} \tag{48}$$

The deformations within the RVE can deviate from the overall deformations. Six degrees of freedom must be suppressed in order to prevent rigid body displacements or rotations of the RVE. Now, any constant stress gradient field can be described by only applying loads on the corner nodes of the FE model.

Forces and moments are applied at the four corner nodes of the RVE to create six elementary load cases. The three in–plane loadcases are: tension in the global x–direction, tension in the y–direction and simple shear in the xy–direction. The three out–of–plane loading conditions are: bending in the global y–direction, bending in the global x–direction and pure twist in the global xy–direction.

The displacements and the reaction forces of the four corner nodes are used to determine the stress and strain state, which are related by the $[abhd]$ compliance matrix. The components of this compliance matrix can be determined directly from the six elementary loadcases.

The thermal properties of the woven fabric composite are determined by pre–stressing the basic elements with the thermally induced element forces and moments from equation (35). The FE model (again subjected to the condition of periodicity) then gives the resulting nodal displacements and rotations of the four corner nodes. These, in turn, lead to the thermal expansion and bending coefficients of the corresponding continuum.

Macro level thermo–elastic modelling

The homogenised RVE properties of the fabric are determined in section . These CLT based properties are relative to the mid–plane of the ply. Stacking of the individual plies results in an offset of each ply to the mid–plane of the composite. This offset has to be accounted for since it affects the CLT properties. The following exercise is performed to derive expressions to account for the offset.

Deriving an expression for the offset The contribution of the individual layers to the composite properties can be derived from the definitions of $[A]$, $[B]$ and $[D]$ in equation (26). Evaluating equation (26) as a ply with homogeneous properties

result in:

$$\begin{aligned}
[A] &= (h_T - h_B)[Q] \\
[B] &= \tfrac{1}{2}({h_T}^2 - {h_B}^2)[Q] \\
[D] &= \tfrac{1}{3}({h_T^k}^3 - {h_B^k}^3)[Q]
\end{aligned} \tag{49}$$

Adding an offset h_o to the height coordinates of the ply h_T and h_B, and substituting these limits in equation (26) followed by integration over the height coordinate results in:

$$\begin{aligned}
[A]^o &= (h_T - h_B)[Q] = [A] \\
[B]^o &= h_o(h_T - h_B)[Q] + \tfrac{1}{2}({h_T}^2 - {h_B}^2)[Q] = h_o[A] + [B] \\
[D]^o &= {h_o}^2(h_T - h_B)[Q] + h_o({h_T}^2 - {h_B}^2)[Q] + \tfrac{1}{3}({h_T}^3 - {h_B}^3)[Q]' \\
&= {h_o}^2[A] + 2h_o[B] + [D]
\end{aligned} \tag{50}$$

where $[A]^o$, $[B]^o$ and $[D]^o$ account for the offset h_o. Similarly, expressions for the loading vectors $\{N\}^o$ and $\{M\}^o$ can be derived. It involves the integration of $\{\sigma(z)\}$ over the height coordinate.

Macro level contribution of the plies The distance between the centre of the composite and the centre of the individual fabric layer is denoted with h_o^k, where k is the ply index. The properties of the individual fabric layer are defined in the xy–coordinate system. However, the individual plies are orientated off–axis in the composite. Rotation of the plies by substituting $[A]^R$, $[B]^R$, $[D]^R$ for $[Q]$ in equation 27 accounts for the ply orientation. The contribution of each individual layer to the composite properties is:

$$\begin{aligned}
[A]^C &= \sum_{k=1}^{m} [A]^{R,k} \\
[B]^C &= \sum_{k=1}^{m} \left(h_o^k [A]^{R,k} + [B]^{R,k} \right) \\
[D]^C &= \sum_{k=1}^{m} \left({h_o^k}^2 [A]^{R,k} + 2h_o^k [B]^{R,k} + [D]^{R,k} \right)
\end{aligned} \tag{51}$$

where the superscript C denotes composite, the superscript R indicates RVE and m is the number of fabric layers in the composite. The thermal properties of the composite are derived similarly to those of the individual layers. Rotation of $\{\tilde{N}\}^R$ and $\{\tilde{M}\}^R$ accounts for the ply orientation. The composite thermal loading vectors

$\{\tilde{N}\}^C$ and $\{\tilde{M}\}^C$ are described as:

$$\begin{aligned}\{\tilde{N}\}^C &= \sum_{k=1}^{m} \{\tilde{N}\}^{R,k} \\ \{\tilde{M}\}^C &= \sum_{k=1}^{m} \left(h_o^k \{\tilde{N}\}^{R,k} + \{\tilde{M}\}^{R,k} \right)\end{aligned} \tag{52}$$

Woven fabric model verification

The thermo–elastic properties of fibre reinforced thermoplastic composites were measured in order to validate the model. Symmetric laminates were manufactured from glass fibre reinforced poly(phenylene sulphide) (PPS) 8H satin weave (Ten Cate Cetex©SS303). All specimens were made by compression moulding, using a Fontijne plate press. The fibre volume fraction in the orthogonal fabric composites was approximately 50%. It was determined prior to compression moulding from the mass fractions of the constituents. The manufacturing technique used for producing the skewed specimens resulted in an increase of the volume fraction with increasing skew angle.

Mechanical testing

Tensile tests were performed using a Zwick type 1445 machine with a 10 kN load cell. Four layered symmetrically builtup specimens with orthogonal weaves, skewed weaves and orthogonal weaves with a Quasi Isotropic (QI) lay–up were tested. The specimens were prepared according to the ASTM D3039–76 protocol [2]. The dimensions of the specimens were 25 mm wide and 250 mm long. The thickness of the specimens was approximately 0.9 mm but varied due the skew angle of the laminates.

The skewed weave specimens were manufactured by placing a dry weave into a shear frame, similar to the picture frame. The areal density of the skewed weave increases since the area of the skewed weave is smaller than the area of the orthogonal weave. A layer of resin foil was placed between the fabric layers. The skewed samples were subsequently moulded in the plate press. The skew angles of the fabric were set at 10°, 20° and 30°. The fibre volume fraction of the skewed specimens is higher than the fibre volume fraction of the orthogonal specimens since the same foil is used for manufacturing. The fibre volume fraction is determined by the following relation:

$$V_{f_s} = \frac{V_f}{(1 - \sin 2\phi)V_f + \sin 2\phi} \tag{53}$$

The specimens with orthogonal weaves were tested in the 0°, 45° and 90° direction with respect to the major principal axis of the material. The specimens with skewed weaves were measured in their bias directions, as depicted in figure 15.

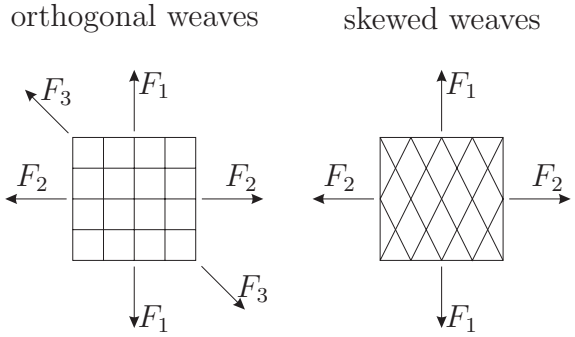

Figure 15: Loading directions for the orthogonal and skewed specimens.

The QI specimens were tested in one direction. The load was directly obtained from the tensile testing machine, while the strain was measured using a clip–on extensiometer. Five tests were performed per type of specimen. The velocity of the tensile testing rig was 1 mm/min. The tests were performed at room temperature. The results will be presented in section , showing a_{11}, the first component of the $[abhd]$ compliance matrix.

Thermal testing

The thermal expansion coefficients of the material were measured in a Thermal Mechanical Analysis (TMA) machine. Basically, the TMA consists of two parts: a high–precision temperature controlled oven, and an accurate displacement measurement device. The test set–up in the TMA is given in figure 16.

The specimen is placed between the probe and the support. Both the probe and the support are made from quarts, a material with a very low thermal expansion. The probe moves vertically and is connected to a Linear Variable Differential Transformer. The whole set–up is placed into a temperature controlled oven and the vertical displacement of the probe is measured as a function of the temperature. The probe loads the specimen with 0.1 N to ensure contact during the measurement. The linear thermal expansion is acquired from the temperature versus displacement curve when the initial thickness is measured.

The symmetrically builtup sixteen layer specimens with a dimension of 29.5 $\times$ 9 $\times$ 4 mm^3 were placed vertically onto the support of the TMA. The samples were dried in a vacuum oven for 3 weeks at a temperature of 50 °Cprior to testing to

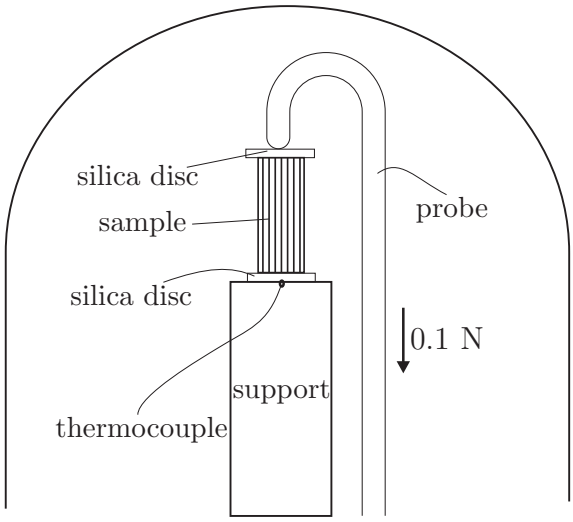

Figure 16: Set–up in TMA for measuring thermal expansion.

eliminate moisture–induced expansion. The thermal cycle, to which the specimen was subjected, is shown in figure 17.

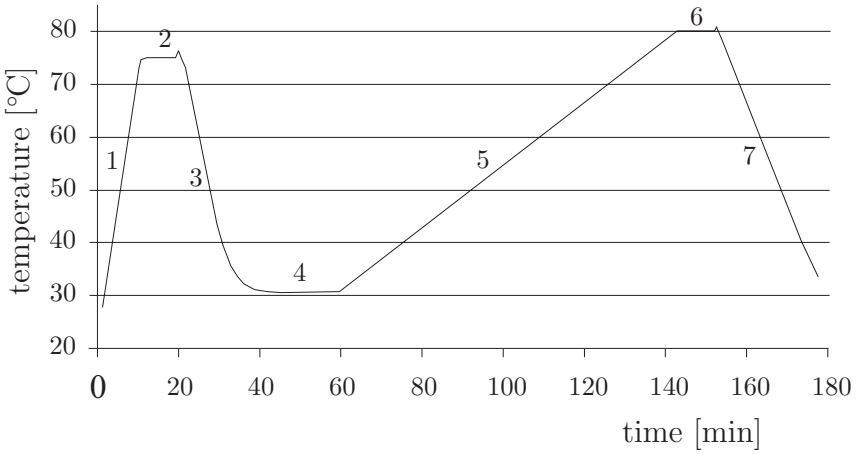

Figure 17: Thermal profile of TMA for measuring thermal expansion.

The TMA cycle program contains seven parts. The first three parts make up one dummy temperature cycle, resulting in less deviation between the individual experimental results. The ramp–up for measuring the thermal expansion was set slow enough to ensure a homogeneous temperature distribution within the specimen.

The results of the thermal expansion measurements will be presented in section .

Results and discussion

Some input parameters are required for modelling the thermo–elastic properties of the weaves. The properties for the 8H satin and the plain weave are obtained from the datasheet from the manufacturer and listed in table 2.

Table 2: Properties of the modelled weaves

property		8H satin	Plain
warp count	1/m	2280	960
fill count	1/m	2200	1050
areal density	kg/m^2	0.3	0.3

The PPS resin material properties are supplied by the manufacturer [18]. The properties of the isotropic E–glass fibres is obtained from literature [22]. An overview of the material input parameters is given in table 3.

Table 3: Properties of the constituents in the composite

property		E-glass	PPS
Young's modulus	GPa	72.4	3.7
Poisson's ratio	-	0.23	0.37
lin. thermal expansion	1/K	5E-6	51E-6
density	kg/m^3	2540	1350

The height of the fabric h_f, the width of the yarns l_{fx} and l_{fy} and the undulated lengths of the yarns U_x and U_y were determined with microscopy investigations of the weaves.

The yarn shape in the plain weave can be fitted with an ellipsoid shape. Most yarn shapes in the cross–section of the plain weave are similar, see figure 18. Little nesting occurred in this weave. However, the yarn shape in the 8H satin weave cross–section are quite dissimilar. Extreme differences in the shape of the yarn, yarn height and width are observed. Nesting of the individual plies is clearly visible in these micrographs.

Optical measurements of the yarns cross–section resulted in the additional parameters. The results are expressed in percentages of the total ply height h_t

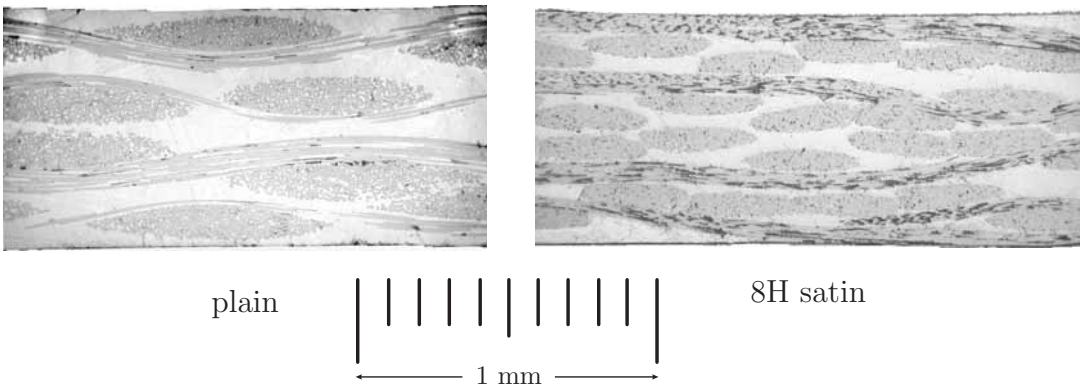

Figure 18: micrographs of the cross–section of a four layered orthogonal plain weave and 8H satin weave.

Table 4: Additional parameters for the woven fabric model.

weave	h_f	l_{fx}	l_{fy}	U_x	U_y
plain	95	85	85	100	100
8H satin	97	90	90	60	60

and total width of the yarns l_x, l_y. The experimental error in these additional parameters is significant.

Mechanical

The experimental results and the modelled results for the unskewed specimens are shown in figure 19. The results are presented in the a_{11} compliance form. A higher a_{11} value indicates a weaker material response.

The laminate is rotated over an angle of 90 ° in the model, illustrating the effect of rotation on the a_{11} properties. Four types of models were used for each weave: the *SS* and *PP* configuration in the averaging approach and the *SS* and *PP* configuration in the FE approach. Tensile tests were performed in the fibre directions (0° and 90 °) and the bias direction (45 °).

The measured a_{11} values is not affected significantly by the weave type. In the fibre directions the *PP* configurations predict these values nicely. The *SS* configurations overestimate the a_{11} values significantly.

A small change in the measured, and modelled, values is determined at the 0° and 90° axis. Since both weaves are not completely regular, a small difference is observed in the 0° and 90° values. Equal results are expected if the weaves are completely

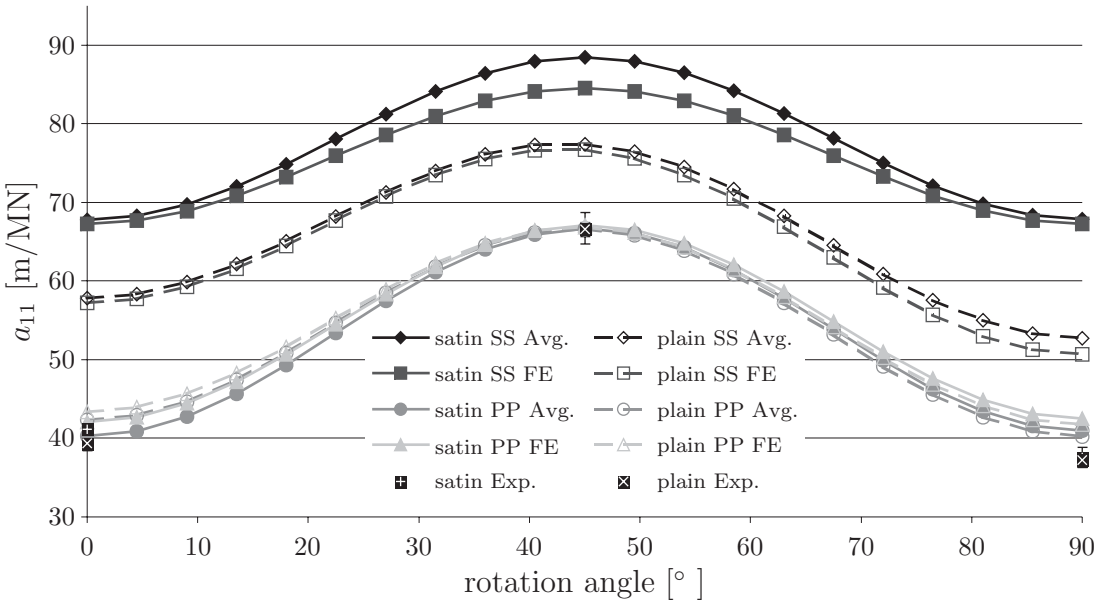

Figure 19: Modelled and experimental values for the a_{11} compliance property of 8H satin and plain weave composites. The enclosed fibre angle of the 4 layered orthogonal composites is denoted in the legend.

regular.

The *PP* or the *SS* configuration predict different results for the plain weave. A difference of approximately 25% is observed between these configurations. The effect of the approach is small; the averaging approach and the FE approach predict nearly the same values in case of the plain weave for the *PP* configuration or the *SS* configuration. This is caused by the homogeneity of the plain weave. Plain weaves consist of *A*–type basic elements only. The strain and stress fields in the FE approach are therefore nearly homogeneous, resulting in similar predictions as the averaging approach.

The results for the satin weave are affected significantly by the *PP* and the *SS* configuration. The difference in the results for the averaging approach is approximately 40% for this weave. The averaging and the FE approach slightly affect the predicted results for the satin 8H weave. The results from the *PP* and *SS* configuration for the averaging approach were further apart for this weave than for the plain weave. This is caused by the less homogeneous basic element distribution of the satin weave; it consists of all basic element types, resulting in a less homogeneous strain and stress field in the FE approach.

The effects of skew deformation on the thermo–elastic properties are shown by performing tensile tests in the bias directions. The results for the plain weave tests

are depicted in figure 20.

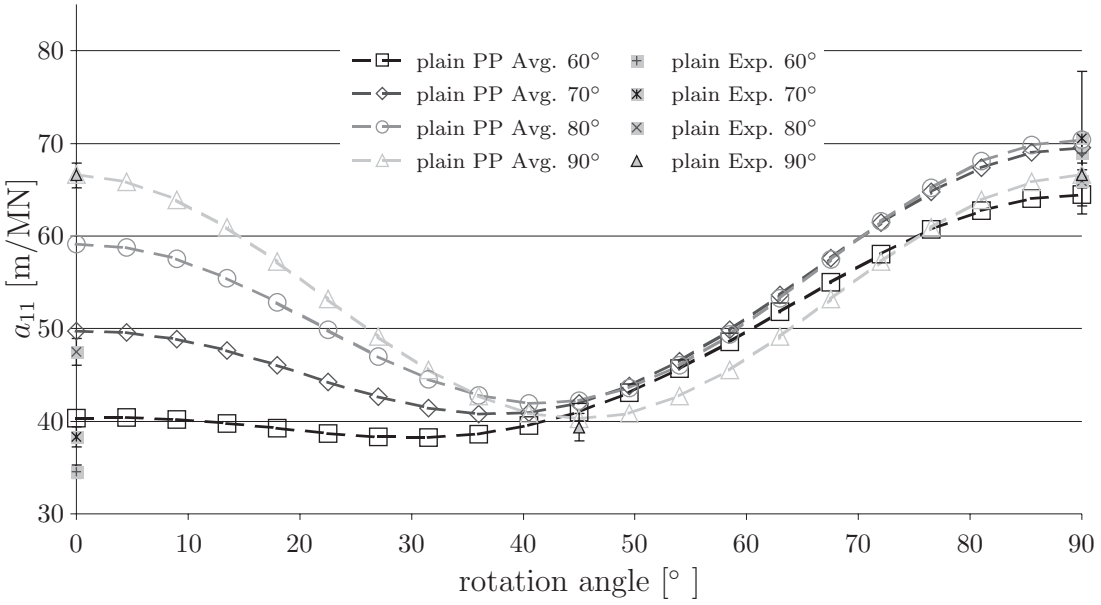

Figure 20: Modelled and experimental values for the a_{11} compliance property of plain weave composites. The enclosed fibre angle of the 4 layered skewed composites is denoted in the legend.

The measured a_{11} values and the predicted results for the *PP* configuration with the averaging approach are shown in figure 20. Again, a_{11} is presented as a function of the rotated angle of the complete laminate. The a_{11} properties of skewed plain weave are affected by the enclosed fibre angle of the weave. A smaller angle results in a significantly lower a_{11} value for the material, *i.e.* the material behaves stiffer. The model overestimates the measured values when the enclosed fibre angle is small. No explanation is found for the overestimation and further investigation of this topic is recommended.

The results for the QI-lay–up laminates are shown in figure 21. The model overestimates the experimental values. Again, the best predictions are obtained with the *PP* configuration with the averaging approach. The experimental plain weave a_{11} property is smaller than those of the 8H satin weave.

The averaging approach predicts the properties more quickly than the FE approach since it does not require to solve the nodal degrees of freedom of the FE mesh. The computing time of the FE approach grows with the size of the unit cell.

The resin material is assumed to be linearly elastic in this analysis. The resin material has however visco–elastic properties. The effect of visco–elasticity on the

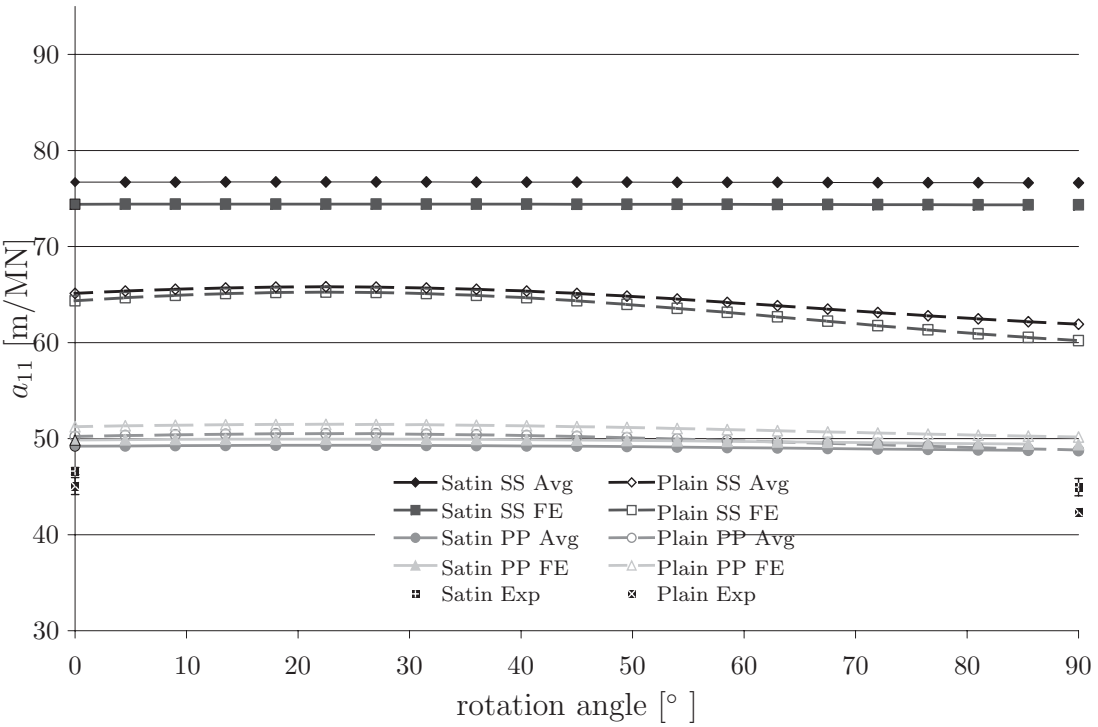

Figure 21: a_{11} property of 8H satin and plain weave 4 layered QI composites.

composite behaviour requires further investigation.

Thermal

The modelled values of the thermal expansion for the unskewed specimens are compared with the measured thermal expansion in figure 22. The thermal expansion was modelled for plain weaves using the averaging approach. A small difference between the measured, and modelled, values is found at the 0° and 90° axis for the in–plane thermal expansion. This difference is caused by the irregularity of the plain weave.

Good agreement between the experimental values and the modelled results is obtained for the orthogonal laminates in both the 0° and the 90° direction. The *SS* configuration overestimates the experimental values in both cases. The better predictions are obtained with the *PP* configuration.

The models predict the coefficients of thermal expansion for QI laminates less well. Both modelled values are outside the experimental error values. Again, the *PP* configuration predicts the experimental values significantly better.

The affect of skew deformation on the thermal expansion of plain weaves was

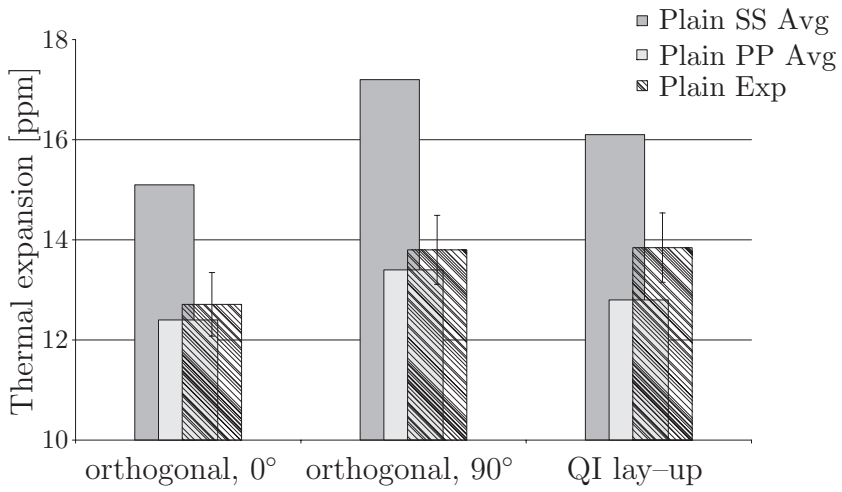

Figure 22: Thermal expansion for an orthogonal plain weave composites and a QI builtup composite.

not experimentally determined. The in–plane thermal expansion of the 8H satin weaves was also not measured. Experiments to validate the model for both weaves is recommended.

Conclusion

A model was presented to determine the in–plane thermo–elastic properties of woven fabric laminates. It provides a good correlation with the experimental results for a plain weave and an 8H satin weave when a uniform state of basic element strain is used (upper bound for the stiffness). In case a uniform state of basic element stress is assumed (lower bound for the stiffness), the laminate stiffness is underestimated.

The bounds for the iso–strain and iso–stress are quite far apart. The difference between the predictions of uniform strain and stress models can be reduced by using an finite element approach. However, applying this FE approach does not increase the accuracy of the model.

The model shows good agreement for the prediction of the thermal expansion of orthogonal weaves in the fibre direction. The thermal expansion of QI laminates is less well predicted but acceptable. As with the elastic properties, the iso–strain configuration predicts the experimental values best.

Recommendations

A few recommendations are suggested for the model to predict the thermo–elastic properties of laminates builtup from non–orthogonal weaves.

The presented model is only validated for in–plane tensile tests and thermal expansion measurements. However, the model presented here predicts the complete ABD stiffness matrix and the thermal expansion–curvature vector. This stiffness matrix includes bending stiffness, represented by the D–matrix and the tension bending coupling, which is accounted for by the B–matrix. Bending tests are recommended in order to validate the predicted D–matrix by model. It is also recommended to extend the validation of the thermal expansion–curvature vector.

The RVE is idealised by a combination of basic elements. The yarn's cross–section, undulation and other geometrically derived properties are defined in these basic elements. Microscopic investigations revealed large differences between the individual yarn geometries. Nesting was also observed in these micrographs. It is recommended to investigate the effect of these differences.

The unidirectional properties of the yarns are predicted by micromechanical models. A large variety of micromechanical models is available in literature. The individual models predict differences up to 100%, especially in the transverse direction. The properties of the yarns, with a high volume fraction, are not experimentally determined and the micromechanical model is therefore not verified. Further work is this area is recommended.

Bibliography

[1] Akkerman, R., and de Vries, R. Thermomechanical properties of woven fabric composites. In *Proceedings of the International Conference on Fibre Reinforced Composites FRC '98, Newcastle, United Kingdom* (1998), A. Gibson, Ed., Woodhead publishing limited, pp. 422–429.

[2] ASTM. Astm d 3039–76. *Annual book of ASTM Standards 08.01* (1989).

[3] Atkinson, K. *An introduction to numerical analysis.* John Wiley & Sons, 1989.

[4] Batoz, J. A study of three–node triangular plate bending elements. *International Journal for Numerical Methods in Engineering 15* (1980), 1771–1812.

[5] Bowles, D., and S.S., T. Prediction of coefficients of thermal expansion for unidirectional composites. *Journal of Composite Materials 23* (1989), 370–388.

[6] Bunsell, A. *Fibre Reinforcements for Composite Materials*, vol. 2 of *Composite Materials Series.* Elesevier, 1988.

[7] Carleer, B. *Finite Element analysis of deep drawing.* PhD thesis, Twente University, March 1997. Ph.D. Thesis, Applied Mechanics Group.

[8] Chamis, C. Nasa tech. memo 8320. *MEMO* (1983).

[9] Chou, T., and Ishikawa, T. Analysis of two dimensional fabric composites. *Textile Structural Composites* (1991), 209–264.

[10] Chou, T., and Ishikawa, T. Mechanics of composite materials. *Textile Structural Composites* (1991), 31–37.

[11] Daniel, I., and Ishai, O. *Engineering Mechanics of Composite Materials.* Oxford University Press, 1994.

[12] Falzon, P., and Herzberg, I. Effects of compaction on the stiffness and strength of plain weave fabric RTM composites. *Journal of Composite Materials 30* (1996), 1211–1247.

[13] Hashin, Z. Analysis of composite materials – a survey. *Journal of Applied Mechanics 50* (1983), 481–505.

[14] Hofstee, J., de Boer, H., and van Keulen, F. Elastic stiffness analysis of thermo–formed plain–weave composite part iii: experimental verification. *Composites Science & Technology 62* (2002), 401–418.

[15] Lamers, E. Review on micromechanical modeling. Tech. rep., Precimould (BE 97-4351), University of Twente, 1999.

[16] Lamers, E. *Shape distortions in fabric reinforced composite products due to processing induced fibre reorientation.* PhD thesis, University of Twente, Enschede, The Netherlands, April 2004.

[17] Lamers, E., Wijskamp, S., and Akkerman, R. Modelling the thermo–elastic properties of skewed woven fabric reinforced composites. In *Proceedings of ECCM 9, Brighton, UK* (2000), pp. CD–proceedings.

[18] Ticona GmbH. *Datasheet Fortron.* Campus V4.1, www.CAMPUSPlatics.com, 1998.

[19] Naik, N., and Shembekar, P. Elastic behaviour of woven fabric composites: I–laminate analysis. *Journal of Composite Materials 26* (1992), 2196–2225.

[20] Naik, N., and Shembekar, P. Elastic behaviour of woven fabric composites: II–laminate analysis. *Journal of Composite Materials 26* (1992), 2227–2246.

[21] Nijhof, A. *Ontwerpen in vezelversterkte kunststoffen.* TU Delft, 1990.

[22] Peters, S. *Handbook of composiets.* Chapman & Hall, 1998.

[23] Powell, P. *Engineering with Fibre–Polymer Laminates.* Chapman & Hall, 1994.

[24] Rosen, B. W., and Hashin, Z. Effective thermal expansion coefficients and specific heats of composite materials. *Journal of Composite Materials 8* (1970), 157–173.

[25] Schapery, R. Thermal expansion coefficients of composite materials based on energy principles. *Journal of Composite Materials 2*, 3 (1968), 380–404.

[26] Schneider, W. Wärmeausdehnungskoeffizienten und wärmespannungen von glassfaser/kuststoff–verbunden. *Kunststoffe 63* (1973), 992.

[27] Vandeurzen, P., Ivens, J., and Verpoest, I. A three dimensional micro mechanical analysis of woven fabric composites: I. elastic analysis. *Composites Science and Technology 56* (1996), 1317–1327.

[28] Vandeurzen, P., Ivens, J., and Verpoest, I. A three dimensional micro mechanical analysis of woven fabric composites: I. geometric analysis. *Composites Science and Technology 56* (1996), 1303–1315.

[29] Whitney, J., and McCullough, R. *Micromechanical Materials Modelling*, vol. 2 of *Delaware composites and design encyclopaedia*. Technomic, Lancaster PA, 1990.

Theoretical background II

UD micromechanics

The next pages contain the theory behind the UD micromechanical models used in U20MM. The part was written within the Brite-Euram project Precimould (BE 97-4351).

University of Twente
Department of Mechanical Engineering
Composites Group

Review
on Micromechanical Modelling

PRECIMOULD (BE97-4351)

doc.nr.: **PREC-UOT-WP8-REP-114**
author: E.A.D. Lamers
date: 29 September 1999
approved: Remko Akkerman

Contents

1 Introduction

In order to predict the thermoelastic properties of continuous fibre reinforced anisotropic composites, micromechanical models are used. The models predict the composite properties from the composite components, the orientation of these components, and the relative distribution of these components. Many of these micromechanical models take the micro structural properties of the matrix material and the fibre material into account to predict the anisotropic properties of the composite material (the fibre shape and the stacking of the individual fibres).
From the various micromechanical models available in the literature, only a few are examined. The examined models differ from purely analytical models to semi-empirical models.

2 Micromechanical modelling

In this chapter, a brief explanation of the theory of micromechanical modelling is done, including an examination of the major effects on the resulting thermoelastic properties of the composite material. After determining the major effects, various micromechanical models are examined.

2.1 Micro-structural approach of composites

In anisotropic composite materials, such as unidirectional fibre reinforced composites, the resulting properties can be described using “combining rules”. In these “combining rules”, the composition, the component properties, and the internal microstructure (fibre size, shape, and packing geometry) are terms to predict the macroscopic properties. However, in order to develop these “combining rules” a microscopic view at the composite material is necessary. In this microscopic view the regions of the composite components should be large enough to be treated as homogeneous continua.
In the micromechanical approach, an internal stress (or strain) field is assumed, that does not contradict the macroscopic stress (or strain) field. The macroscopic stress-strain filed is defined by a load-deformation pattern, imposed on the boundaries of the composite. The internal stress-strain field, resulting from the macroscopic stress-strain field, acts on both phases and their boundaries in the microstructure.
The major effects on the internal stress-strain field can be distinguished as

1. The relative magnitudes of the properties of the two components.
2. The size, shape, and relative orientation of the two phase regions.
3. The packing geometry of the phase regions.

A brief examination of these effects will be done in the next paragraphs.

2.1.1 The relative magnitudes of the component properties

The internal stress-strain field is influenced by the relative properties of the two components. Large relative differences between properties of the two components result in large differences in the internal stress-strain field.
To clarify this, the following example is shown:
Combining stiff fibres in a weak matrix results in a stress-strain field that differs from a stress-strain field where the relative difference between fibre and matrix properties are less large.

2.1.2 The size, shape and relative orientation of the two phases

The size, shape, and relative orientation of the two-phase regions have influence on the internal stress-strain field resulting form the macroscopic stress-strain field.
The relative amounts of the components obviously influence the resulting stress-strain filed. The shape of the phases, influenced by each other, also have influence on the internal stress-strain field. Combining, for example, square or circular fibres in a composite obviously influences the resulting internal stress-strain field. Also, the orientations of the phases have influence on the resulting stress-strain field. Even the phases them selves can have non-isotropic properties.

2.1.3 Packing geometry of the phase regions

The fibres in a composite can be packed in numerously ways. The fibre distribution can be homogeneous or non- homogeneous. The way fibres are distributed therefore have influence on the internal stress-strain field.

Some examples of fibre distribution are shown in figure 1. Depending on the fibre packing, different results for the mechanical properties of the composite can be measured. Therefore, to obtain accurate results for predicting the composite properties, micromechanical models should take the fibre packing into account.

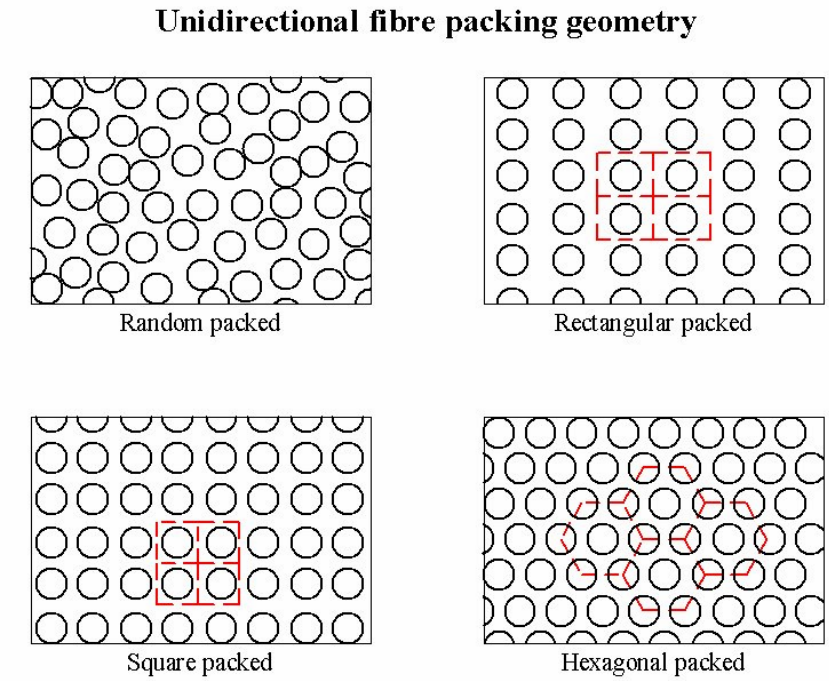

figure 1: Unidirectional fibre packing geometry

As shown in figure 1, each fibre packing geometry has its own fibre volume fraction. The theoretically maximum fibre volume fraction for circular fibres is calculated in the next paragraph.

2.1.4 Maximum possible fibre volume fraction

For the homogeneously distributed circular fibres, the theoretical maximum fibre volume fraction can be calculated. The maximum value for the fibre volume fraction depends on the fibre packing geometry. The theoretically possible fibre volume fractions of two types of packing geometry are examined in this paragraph, the fibre volume fraction for the square packed fibres and the hexagonal fibres.
In figure 2, the maximum amount of circular fibres is packed into a composite.

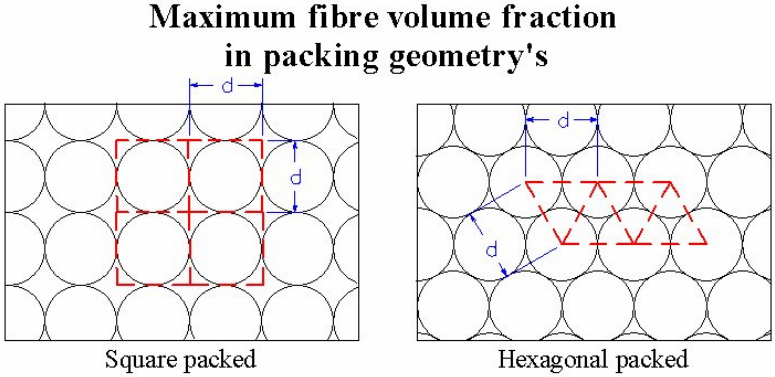

figure 2: Maximum fibre volume fraction in packing geometries

The mathematically representation of the fibre volume fraction of the packing geometries shown in figure 2, are given in the equations below. Equation 2-1 gives the maximum fibre volume fraction for square packing, and equation 2-2 gives the maximum fibre volume fraction for hexagonal packing.

$$V_{f\max} = \frac{\pi.d^2}{4.d^2} = \frac{\pi}{4} \approx 0.7854 \quad \text{, for square packing} \qquad \textbf{2-1}$$

$$V_{f\max} = \frac{\pi.d^2}{4.\frac{1}{2}\sqrt{3}.d^2} = \frac{\pi}{2.\sqrt{3}} \approx 0.9096 \quad \text{, for hexagonal packing} \qquad \textbf{2-2}$$

In equations 2-1 and 2-2, $V_{f\,max}$ is the maximum fibre volume fraction and d is the fibre diameter.

2.2 Micromechanical models

Two types of predictions will be examined; models that predict the elastic properties and models that predict the linear thermal expansion coefficient. However, splitting the models into two types does not imply that the models are based on another theoretical approach. The predictions from, for example, the *Rule of Mixtures* models for elastic properties are based on exactly the same approach as the *Rule of Mixtures* models for the prediction of the linear thermal expansion coefficient.

2.2.1 Models for elastic properties

In this section, models that predict the elastic properties of continuous fibre reinforced composite materials are examined. The models that will briefly be discussed here are the *Rule of Mixtures* models, *Composite Cylinder Assemblage* (CCA) model, the *Chamis* models, the *Puck* model and the semi-empirical *Halpin-Tsai* models.

2.2.1.1 Rule of Mixtures models

The Rule of Mixture models, based on the mechanics of materials approach [1], are the two most basic models available for prediction of the composite properties from the properties of the matrix material, the fibre material and the fibre volume fraction. It does not take the fibre shape or the fibre distribution into account. The models assume perfect bonding between the matrix material and the fibre material. The matrix material and the fibre material are assumed orthotropic and can be simplified to the isotropic case.
The models can either assume uniform strain on each of the components (parallel model) or uniform stress on each of the components (series model) in the composite material at micro level.
In the fibre direction a uniform strain is assumed and perpendicular to this direction a uniform stress is assumed [2]. The results obtained with these models are shown in table 1:

Property	**Mathematical equation**
Longitudinal modulus	$E_{cL} = E_{fL}.V_f + E_{mL}.V_m$
Transverse modulus	$\frac{1}{E_{cT}} = \frac{V_m}{E_{mT}} + \frac{V_f}{E_{fT}}$

In-plane shear modulus	$\frac{1}{G_{cLT}} = \frac{V_m}{G_{mLT}} + \frac{V_f}{G_{fLT}}$
In-plane Poisson ratio	$\nu_{cLT} = \nu_{fLT}.V_f + \nu_{mLT}.V_m$
	with $V_f = 1 - V_m$

table 1: Elastic properties using *Rule of Mixtures* models

The "longitudinal" Rule of Mixtures model generally gives very good predictions in the fibre direction (longitudinal modulus and Poisson ratio). Transverse to the fibre direction, the "transverse" Rule of Mixtures model underestimates the properties of the composite material (transverse modulus and in-plane shear modulus).

2.2.1.2 CCA model

This model, based on the self-consistent field (or embedding) method, simplifies the microstructure of the composite. The method is based on transversely isotropic composite materials. The method however deals in a more realistic way with the internal stresses in a composite than the micromechanical approach [1].
By embedding continuos fibres in a concentric matrix, Hashin [3, 4] formulated and solved the mathematical solutions for this model, called the Composite Cylinder Assemblage. The model gives the exact properties for E_{cL}, G_{cLT}, ν_{cLT}, and close bounds for E_{cT} and G_{cTT}. The resulting equations are shown in table 2.

Property	**Mathematical equation**	
Longitudinal modulus	$E_{cL} = E_{fL}.V_f + E_{mL}.V_m + \dfrac{4(\nu_{fLT} - \nu_{mLT})^2 V_m V_f}{V_m/k_f + V_f/k_m + 1/G_{mTT}}$	
	where	$k = \dfrac{k_m(k_f + G_{mTT}).V_m + k_f(k_m + G_{mTT}).V_f}{(k_f + G_{mTT}).V_m + (k_m + G_{mTT}).V_f}$
	and	$\dfrac{1}{k_f} = -\dfrac{1}{G_{fTT}} - \dfrac{4\nu_{fLT}^2}{E_{fL}} + \dfrac{4}{E_{fT}}$ $\dfrac{1}{k_m} = -\dfrac{1}{G_{mTT}} - \dfrac{4\nu_{mLT}^2}{E_{mL}} + \dfrac{4}{E_{mT}}$
In-plane shear modulus	$G_{cLT} = G_{mLT}.\dfrac{G_{mLT}.V_m + G_{fLT}(1+V_f)}{G_{mLT}(1+V_f) + G_{fLT}.V_m}$	
In-plane Poisson ratio	$\nu_{cLT} = \nu_{fLT}.V_f + \nu_{mLT}.V_m + \dfrac{4(\nu_{fLT} - \nu_{mLT})(1/k_m - 1/k_f)V_m.V_f}{V_m/k_f + V_f/k_m + 1/G_{mTT}}$	
Transverse shear modulus	when $G_{fTT} > G_{mTT}$ and $k_f > k_m$	$G_{cTT(-)} = G_{mTT} + \dfrac{V_f}{\left\{\dfrac{1}{G_{fTT} - G_{mTT}} + \dfrac{(k_m + 2G_{mTT})V_m}{2G_{mTT}(k_m + G_{mTT})}\right\}}$ $G_{cTT(+)} = G_{mTT}\left(1 + \dfrac{(1+\beta_1)V_f}{\partial - V_f\left\{1 + (3\beta_1^2 V_m^2)/(\alpha V_f^3 + 1)\right\}}\right)$
Transverse shear modulus	else	$G_{cTT(-)} = G_{mTT} + \dfrac{V_f}{\left\{\dfrac{1}{G_{fTT} - G_{mTT}} + \dfrac{(k_m + 2G_{mTT})V_m}{2G_{mTT}(k_m + G_{mTT})}\right\}}$ $G_{cTT(+)} = G_{mTT}\left(1 + \dfrac{(1+\beta_1)V_f}{\partial - V_f\left\{1 + (3\beta_1^2 V_m^2)/(\alpha V_f^3 - \beta_1)\right\}}\right)$
Transverse modulus	$E_{cT(+)} = \dfrac{4kG_{cTT(\pm)}}{k + mG_{cTT(\pm)}}$ where $m = 1 + \dfrac{4k\nu_{cLT}^2}{E_{cL}}$	
	with $V_f = 1 - V_m$ $\alpha = \dfrac{\beta_1 - \gamma\beta_2}{1 + \gamma\beta_2}$ $\quad \partial = \dfrac{\gamma + \beta_1}{\gamma - 1}$ $\beta_1 = \dfrac{k^m}{k^m + 2G_{TT}^m}$ $\quad \beta_2 = \dfrac{k^f}{k^m + 2G_{TT}^f}$ $\gamma = \dfrac{G_{TT}^f}{G_{TT}^m}$	

table 2: Elastic properties using *Composite Cylinder Assemblage* model

The *CCA* model predicts the same values for the composite properties in the fibre direction as the *Rule of Mixtures* model. Transverse to the fibre direction, the *CCA* model should predict the composite properties better than the *Rule of Mixtures* model.

2.2.1.3 Chamis

Chamis [5] has summarised the elastic properties for transversely isotropic unidirectional continuous fibre reinforced composites based on the elastic properties of the constituents. Assuming transversely isotropic composite properties, five independent composite properties can be described. The same five properties can be found when assuming a hexagonal packing geometry of the fibres in the composite (hexagonal symmetry) [6].
In general, his work can be applied in the two directions perpendicular to the fibre direction. He treats the fibre as an anisotropic material, while he assumes the matrix to be isotropic. Again perfect bonding between the matrix and the fibre is assumed.
The resulting equations are shown in table 3.

Property	**Mathematical equation**
Longitudinal modulus	$E_{cL} = E_{fL}.V_f + E_{mL}.V_m$
Transverse modulus	$E_{cT} = \frac{E_m}{1 - \sqrt{V_f(1 - \frac{E_m}{E_{fT}})}}$
In-plane shear modulus	$G_{cLT} = \frac{G_m}{1 - \sqrt{V_f(1 - \frac{G_m}{G_{fLT}})}}$
Transverse shear modulus	$G_{cTT} = \frac{G_m}{1 - \sqrt{V_f(1 - \frac{G_m}{G_{fTT}})}}$
In-plane Poisson ratio	$\nu_{cLT} = \nu_{fLT}.V_f + \nu_{mLT}.V_m$
Transverse Poisson ratio	$\nu_{cTT} = \frac{E_{cT}}{2.G_{cTT}} - 1$
	with $V_f = 1 - V_m$

table 3: Elastic properties using *Chamis* models

As the *Rule of Mixtures* model and the *CCA* model, the models summarised by Chamis predict the same values for the composite longitudinal properties. Transverse to the fibre direction the models should predict better values for the composite properties than the *Rule of Mixtures* model.

2.2.1.4 Puck

Puck also derived some models to predict elastic properties of unidirectional fibre reinforced composites, based on the properties of its constituents [7]. His work is based on glass fibre reinforced composites and therefore, the *Puck* model assumes isotropic material properties from the fibre material, as well as the matrix material. The results are shown in table 4.

Property	**Mathematical equation**

Longitudinal modulus	$E_{cL} = E_f.V_f + E_m.V_m$
Transverse modulus	$E_{cT} = E_m.\frac{1+0.85V_f^2}{V_f.\frac{E_m}{E_f}+(1+\nu_m^2).V_m^{1.25}}$
In-plane shear modulus	$G_{cLT} = G_m.\frac{1+0.6V_f^{0.5}}{V_f.\frac{G_m}{G_f}+V_m^{1.25}}$
In-plane Poisson ratio	$\nu_{cLT} = \nu_f.V_f + \nu_m.V_m$
	with $V_f = 1 - V_m$

table 4: Elastic properties using *Puck* models

The *Puck* model is originally derived for glass fibre reinforced composites. The model therefore is based on isotropic materials. The predicted results in the fibre direction are again the same as those predicted using the *Rule of Mixtures* model.

2.2.1.5 Halpin-Tsai

Halpin and Tsai derived a semi-empirical relationship that relates "series-coupled" and "parallel-coupled" models using a scale factor. This scale factor can be used to 'fit' the model to the experimental value for a property.
The model can be directly derived from the mechanics of materials approach, as shown by McCullough [ ]. The general form of the relationship is shown in equations 2-3.

$$P = \frac{P_m(1+\xi.\chi.V_f)}{1-\chi.V_f} \qquad \text{with } \chi = \frac{P_f - P_m}{P_f + \xi.P_m} \qquad \textbf{2-3}$$

In equation 2-3, P_c is the resulting composite property, P_m is the associating matrix property and P_f is the associating fibre property. The parameter ξ is the reinforcing factor, a measure of the "reinforcing efficiency" of the composite material system. This "reinforcing efficiency" can be used to fit the model to the experimental value. When the "reinforcing efficiency" is zero, the model converges to the "series-coupled" model, which equals the *"transverse" Rule of Mixtures*. However, if the "reinforcing efficiency" is infinitely, the *Halpin-Tsai* model converges to the "parallel-coupled" model, which equals the *"longitudinal" Rule of Mixtures*. Also the model can be scaled for any fibre arrangements, fibre shape, or bonding efficiency between fibre and matrix by this "reinforcing efficiency".
The most commonly used equations for conservative estimations of continuous fibre reinforced composites are shown in table 5.

Property	Mathematical equation
Longitudinal modulus	$E_{cL} = E_{fL}.V_f + E_{mL}.V_m$
Transverse modulus	$E_{cT} = \frac{4.k_{cT}.G_{cTT}.E_{cL}}{E_{cL}.(k_{cT} + G_{cTT}) + 4.k_{cT}.G_{cTT}.\nu_{cLT}^2}$
	where $k_{cT} = \frac{k_{mT}.k_{fT} + G_{mT}.(k_{mT} + V_f.(k_{fT} - k_{mT}))}{k_{fT}.V_m + k_{mT}.V_f + G_{mT}}$
In-plane shear modulus	$G_{cLT} = \frac{G_{mLT}.(G_{fLT}.(1+V_f) + G_{mLT}.V_m)}{G_{mLT}.(1+V_f) + G_{fLT}.V_m}$
Transverse shear modulus	$G_{cTT} = \frac{G_{mTT}.\left(1 - \frac{k_{mT}.V_f.(G_{mTT} - G_{fTT})}{G_{fTT}.k_{mT}+2.G_{fTT}.G_{mTT}+k_{mT}.G_{mTT}}\right)}{1 + \frac{(G_{mTT} - G_{fTT}).(k_{mT} + 2.G_{mTT}).V_f}{G_{fTT}.k_{mT}+2.G_{fTT}.G_{mTT}+k_{mT}.G_{mTT}}}$
In-plane Poisson ratio	$\nu_{cLT} = \nu_{fLT}.V_f + \nu_{mLT}.V_m$
Transverse Poisson ratio	$\nu_{cTT} = 1 - \frac{E_{cT}}{2.k_{cT}} - 2.\nu_{cLT}^2.\frac{E_{cT}}{E_{cL}}$
	with $V_f = 1 - V_m$

table 5: Elastic properties using *Halpin-Tsai* models

Using the "reinforcing efficiency" factor, the Halpin-Tsai equations can be fitted to any experimental value. The models can be modified to fit the *Rule of Mixtures*, and predict accurate results in the fibre direction. Transverse to the fibre directions, the model can either be stiffened of weakened to fit the experimental values.

2.2.2 Models for linear thermal expansion properties

In this section, models that predict the thermal properties of continuous fibre reinforced composite materials are examined. The models that will briefly be discussed here are the *Rule of Mixtures models*, the *Shapery* model, the *Chamis* and *CCA* models, the *Schneider* model and the *Chamberlain* models.

2.2.2.1 Rule of Mixtures models

These models predict the linear thermal expansion coefficient in the fibre direction and transverse to the fibre direction. The methods are based on the mechanics of materials approach and give results similar to those described in paragraph 2.2.1.1. The results obtained with these models are shown in table 6:

Property	**Mathematical equation**
Longitudinal linear thermal expansion coefficient	$\alpha_{cL} = \frac{\alpha_{fL}.E_{fL}.V_f + \alpha_{mL}.E_{mL}.V_m}{E_{fL}.V_f + E_{mL}.V_m}$
Transverse linear thermal expansion coefficient	$\alpha_{cT} = \alpha_{fT}.V_f + \alpha_{mT}.V_m$
	with $V_f = 1 - V_m$

table 6: Thermal expansion using *Rule of Mixtures* models

The "longitudinal" *Rule of Mixtures* model generally gives reasonable approximations for the linear thermal expansion coefficient in the fibre direction. Transverse to the fibre direction however, the "transverse" *Rule of Mixtures* model predicts the linear thermal expansion coefficient less good.

2.2.2.2 Shapery

Based on energy principles, *Shapery* [8] derived models for the prediction of the linear thermal expansion coefficient for composite materials. In his work, he confirms the validity of the "longitudinal" *Rule of Mixtures*. For the transverse direction, he derived a linear thermal expansion coefficient depending on the longitudinal expansion coefficient.

Property	**Mathematical equation**
Longitudinal linear thermal expansion coefficient	$\alpha_{cL} = \frac{\alpha_{fL}.E_{fL}.V_f + \alpha_{mL}.E_{mL}.V_m}{E_{fL}.V_f + E_{mL}.V_m}$
Transverse linear thermal expansion coefficient	$V_f < \frac{1}{4}$: $\alpha_{cT} = (1+\nu_{mLT})\alpha_{mT}.V_m + (1+\nu_{fLT})\alpha_{fT}.V_f - \alpha_{cL}.\nu_{cLT}$
	$V_f \geq \frac{1}{4}$: $\alpha_{cT} = (1+\nu_{mLT})\alpha_{mT}.V_m + \alpha_{fT}.V_f$
	with $V_f = 1 - V_m$

table 7: Thermal expansion using *Shapery* models

The *Shapery* models predict in the fibre direction the same value as the "longitudinal" *Rule of Mixtures* model and gives a reasonable approximation for the linear thermal expansion coefficient. Transverse to the fibre direction, the *Shapery* model should predict better approximations for the linear thermal expansion coefficient than the *Rule of Mixtures* model.

2.2.2.3 Chamis and CCA

The results from the *Chamis* models for predictions of the linear thermal expansion coefficient correspondent with the results obtained with the *CCA* models for the linear thermal expansion coefficient derived by Hashin and Rosen. The resulting equations are shown in table 8.

Property	Mathematical equation
Longitudinal linear thermal expansion coefficient	$\alpha_{cL} = \frac{\alpha_{fL}.E_{fL}.V_f + \alpha_{mL}.E_{mL}.V_m}{E_{fL}.V_f + E_{mL}.V_m}$
Transverse linear thermal expansion coefficient	$\alpha_{cT} = \alpha_{fT}.\sqrt{V_f} + \alpha_m.(1-\sqrt{V_m}).\left(1 + \frac{V_f.V_m.E_{fL}}{E_{fL}.V_f + E_m.V_m}\right)$
	with $V_f = 1 - V_m$

table 8: Thermal expansion using *Chamis* models

The *Chamis* model predicts in the fibre direction the same value as the "longitudinal" *Rule of Mixtures* model and gives a reasonable approximation for the linear thermal expansion coefficient. Transverse to the fibre direction, the *Chamis* model should predict better approximations for the linear thermal expansion coefficient than the *Rule of Mixtures* model.

2.2.2.4 Schneider

Schneider derived some models for the prediction of the linear thermal expansion coefficient for continuous fibre reinforced composites [9]. His work however, is based on glass fibre reinforced composites. Therefore, the *Schneider* model assumes isotropic material properties from the fibre material, as well as the matrix material. The results of his wok are shown in table 9.

Property	Mathematical equation
Longitudinal linear thermal expansion coefficient	$\alpha_{cL} = \frac{\alpha_f.E_f.V_f + \alpha_m.E_m.V_m}{E_f.V_f + E_m.V_m}$
Transverse linear thermal expansion coefficient	$\alpha_{cT} = \alpha_m - (\alpha_m - \alpha_f).\left(A + \frac{\nu_m.\frac{E_f}{E_m}}{\frac{E_f}{E_m} + \frac{(1-1.1V_f)}{1.1V_f}}\right)$
	with $A = \frac{2.2(\nu_m^2 - \nu_m - 1)V_f}{1.1V_f.(2\nu_m^2 + \nu_m - 1) - (1+\nu_m)}$ $V_f = 1 - V_m$

table 9: Thermal expansion using *Schneider* models

The *Schneider* model is originally derived for glass fibre reinforced composites. The model therefore is based on isotropic materials. In the fibre direction the *Schneider* model predicts the same value as the *Rule of Mixtures* model.

2.2.2.5 Chamberlain

Chamberlain [10] derived equations for the linear thermal expansion coefficient, based on carbon reinforced unidirectional composites. He assumed transversely isotropic fibres in an isotropic matrix material. He derived two results for the transverse linear thermal expansion coefficient, depending on the packing geometry of the fibres in the composite. The packing geometries he dealt with are the hexagonal and the square packing geometry. The results of his work are shown in table 10.

Property	**Mathematical equation**
Longitudinal linear thermal expansion coefficient	$\alpha_{cL} = \frac{\alpha_{fL}.E_{fL}.V_f + \alpha_m.E_m.V_m}{E_{fL}.V_f + E_m.V_m}$
Transverse linear thermal expansion coefficient	$\alpha_{cT} = \alpha_m + \frac{2V_f.(\alpha_m - \alpha_f)}{\nu_m(F-1+V_m) + F + V_f + \frac{E_m.(1-\nu_{fLT})(F-1+V_m)}{E_{fL}}}$
	with F = 0.9069 for hexagonal disposition F = 0.7854 for square disposition $V_f = 1 - V_m$

table 10: Thermal expansion using *Chamberlain* models

In the fibre direction the *Chamberlain* model predicts the same value as the *Rule of Mixtures* model. The model has been successfully used for experimental verification with carbon reinforced composites by Rogers et al. [11].

3 Comparison between models and measured values

In this chapter, a comparison between a reference material and the micromechanical models is made. First the reference material is presented, and then the comparison is made.

3.1 Reference material

To verify the micromechanical models, measurements of unidirectional composite materials are necessary. As a reference, a unidirectional composite consisting of E-glass [12] and Epoxy [13] (properties shown in table 11) is chosen. The measured values of the elastic and thermal properties of the composite are found in the literature [14] and shown in table 11.

Material property	**Unit**	**E-Glass**	**Epoxy**	**Composite**
Fibre Volume Fraction	[%]	100	0	55
Longitudinal modulus	[Gpa]	72.4	3.24	39
Transverse modulus	[Gpa]	72.4	3.24	8.6
In-plane Shear modulus	[Gpa]	30.2	1.27	3.8
In-plane Poisson ratio		0.2	0.276	0.28
Longitudinal linear thermal expansion coefficient	[1/K]	5E-6	66E-6	7.0E-6
Transverse linear thermal expansion coefficient	[1/K]	5E-6	66E-6	21E-6

table 11: Properties of E-Glass, Epoxy and E-Glass/Epoxy composite

As shown in table 11, E-Glass and Epoxy are isotropic materials. In real-life applications however, carbon fibres are often implemented as a reinforcing material. Carbon fibres however are non-isotropic and the transverse properties of fibres are hard to determine. Often, micromechanical models are used to determine these transverse fibre properties. Therefore, to verify the results of the micromechanical models, isotropic materials are used.

3.2 Comparison between the models and the reference composite

In this paragraph, the micromechanical models are compared with a reference material. The micromechanical models are programmed in a C++ micromechanical ATL COM application [15]. By doing so, these micromechanical models are available for use in various applications. Not all the elastic properties have been verified in this review, unfortunately for some of the modelled properties no verifying measurements were available.
First the predicted elastic properties will be verified, then the predicted thermal properties.

3.2.1 Comparison of elastic properties

In this paragraph, the predicted elastic properties will be compared with the reference properties of an E-Glass/Epoxy composite material. The verified elastic properties are E_{cL}, E_{cT}, ν_{cLT} and G_{cLT}. All properties will be examined in their respective order.

3.2.1.1 Comparison of E_{cL}

In this paragraph, the predicted longitudinal modulus E_{cL} is compared with an experimental value for E_{cL}. In figure 3 the composite longitudinal modulus is shown as a function of the fibre volume fraction.

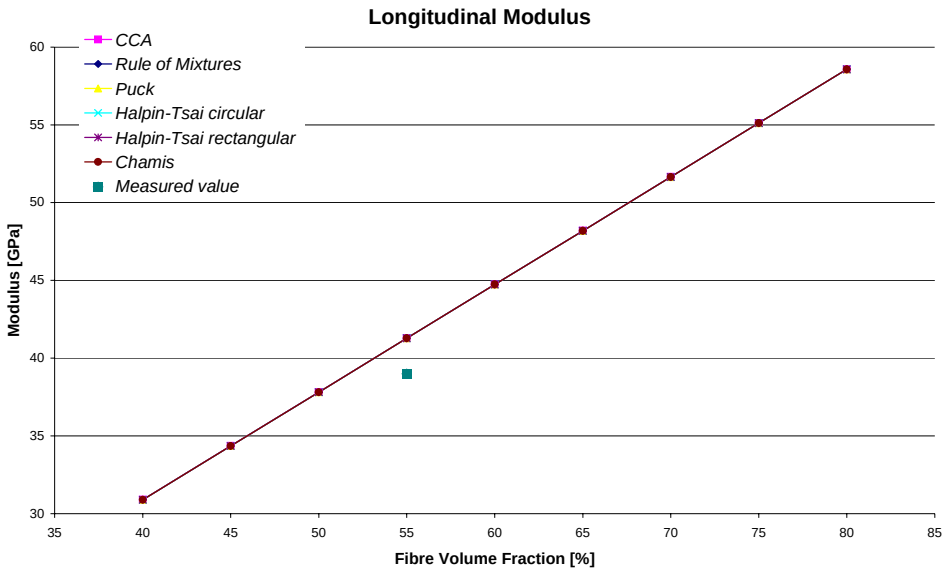

figure 3: Longitudinal modulus

From figure 3, it is clear that all models predict the same longitudinal modulus. The predicted modulus is slightly higher than the experimental value for the composite longitudinal modulus.

3.2.1.2 Comparison of E_{cT}

In this paragraph, the predicted transverse modulus E_{cT} is compared with an experimental value for E_{cT}. In figure 4 the composite transverse modulus is shown as a function of the fibre volume fraction.

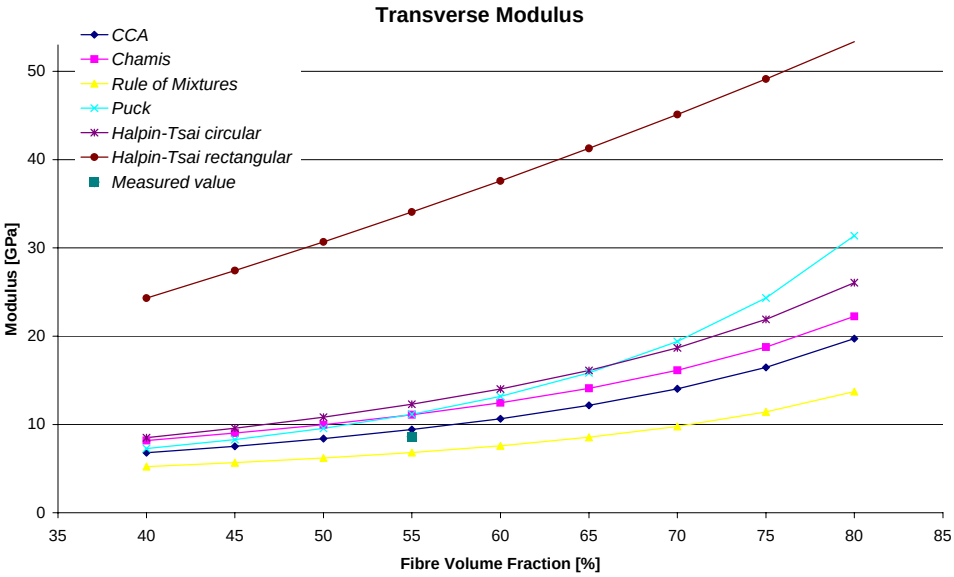

figure 4: Transverse modulus

From figure 4, it becomes clear that the *Composite Cylinder Assemblage (CCA)* model predicts the best value for the transverse modulus compared with the experimental value. The *CCA* model slightly over estimates the value, while the *Rule of Mixtures* model underestimates the experimental value. The other models, *Chamis*, *Halpin-Tsai* and *Puck* increasingly overestimate the experimental value for the composite transverse modulus.

3.2.1.3 Comparison of G_{cLT}

In this paragraph, the predicted in-plane modulus G_{cLT} is compared with an experimental value for G_{cLT}. In figure 5 the composite in-plane shear modulus is shown as a function of the fibre volume fraction.

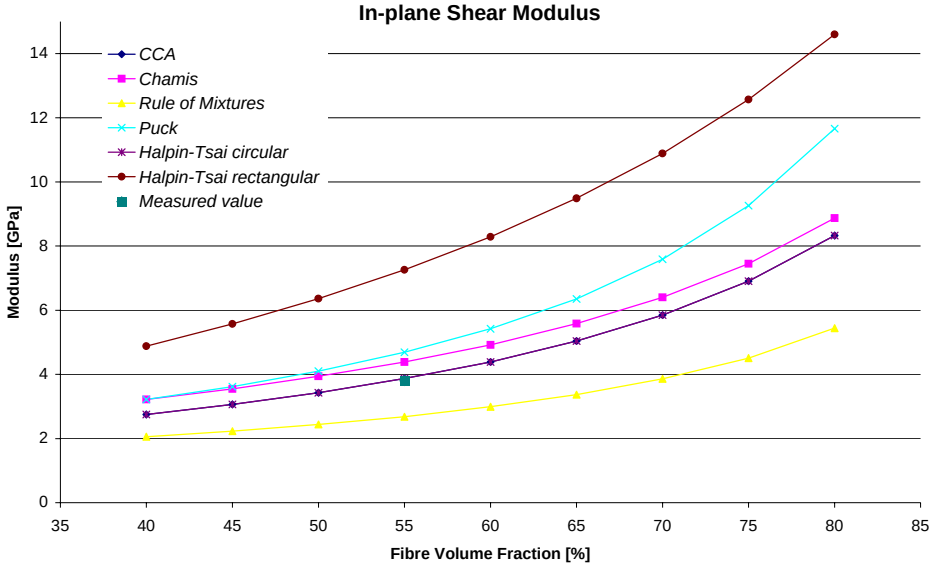

figure 5: In-plane shear modulus

From figure 5, it becomes clear that the *Composite Cylinder Assemblage (CCA)* model predicts the best value for the in-plane shear modulus compared with the experimental value. The *CCA* model slightly over estimates the value, while the *Rule of Mixtures* model underestimates the experimental value. The other models, *Chamis*, *Halpin-Tsai* and *Puck* increasingly overestimate the experimental value for the composite in-plane shear modulus.

3.2.1.4 Comparison of ν_{cLT}

In this paragraph, the predicted in-plane Poisson constant ν_{cLT} is compared with an experimental value for ν_{cLT}. In figure 6 the composite in-plane Poisson constant is shown as a function of the fibre volume fraction.

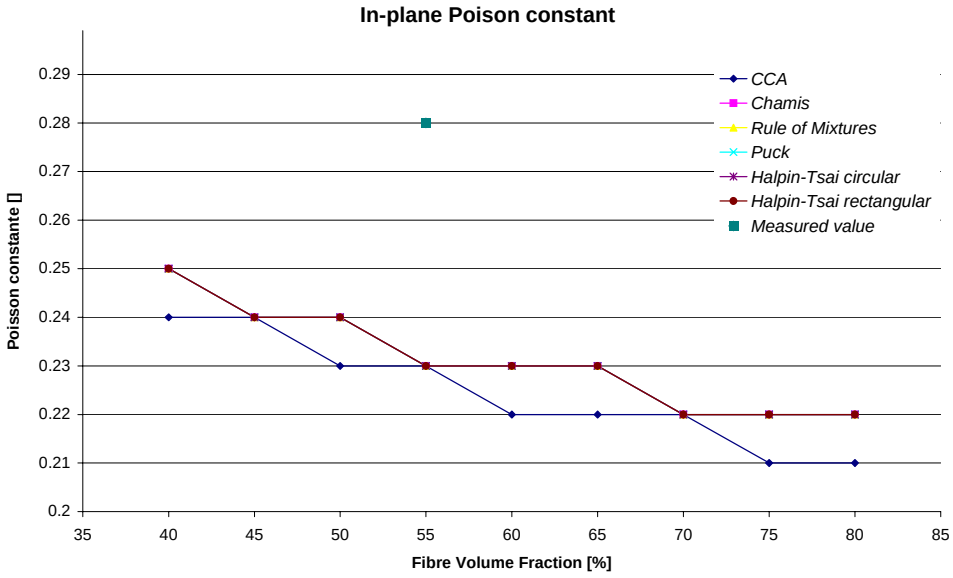

figure 6: In-plane Poisson constant

From figure 6, it becomes clear that all the models give approximately the same prediction. The models underestimate the experimental value for the in-plane Poisson constant.

3.2.2 Comparison of thermal properties

In this paragraph, the predicted thermal properties (α_{cL} and α_{cT}) will be compared with the reference properties of an E-Glass/Epoxy composite material.

3.2.2.1 Comparison of α_{cL}

In this paragraph, the predicted longitudinal linear thermal expansion coefficient α_{cL} is compared with an experimental value for α_{cL}. In figure 7 the composite longitudinal linear thermal expansion coefficient is shown as a function of the fibre volume fraction.

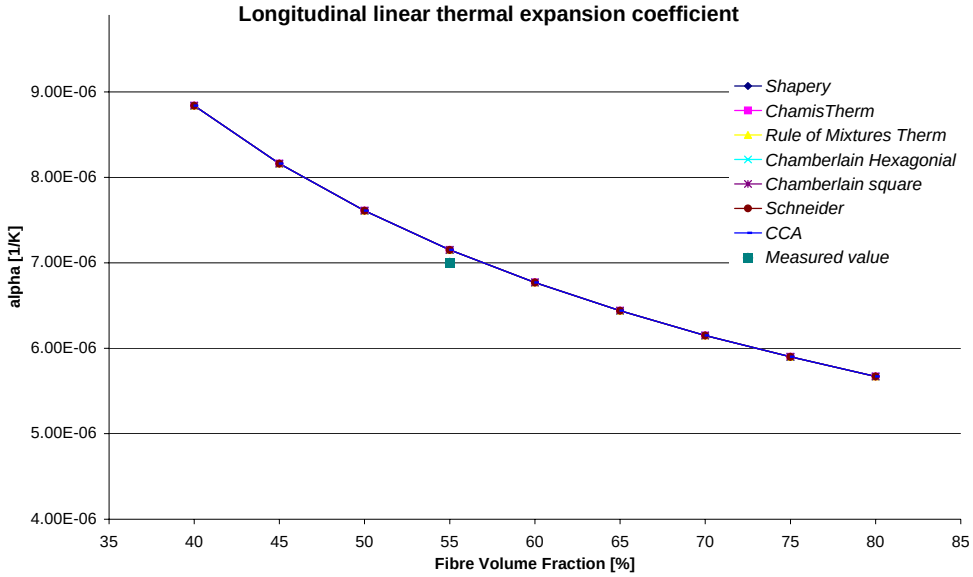

figure 7: Longitudinal linear thermal expansion coefficient

From figure 7, it is clear that all models predict the same longitudinal linear thermal expansion coefficient. The predicted value is slightly higher than the experimental value for the composite longitudinal linear thermal expansion coefficient.

3.2.2.2 Comparison of α_{cT}

In this paragraph, the predicted transverse linear thermal expansion coefficient α_{cT} is compared with an experimental value for α_{cT}. In figure 8 the composite transverse linear thermal expansion coefficient is shown as a function of the fibre volume fraction.

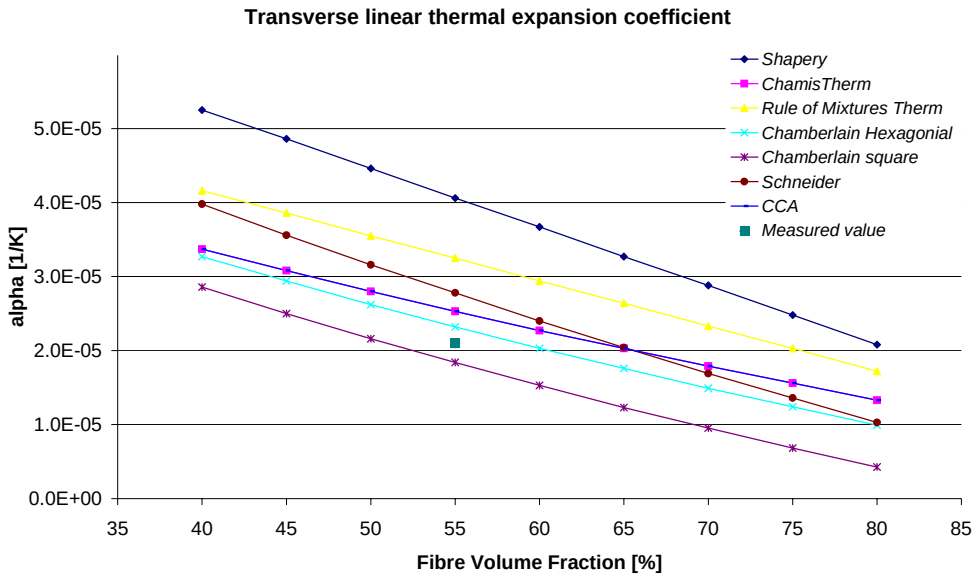

figure 8: Transverse linear thermal expansion coefficient

From figure 8, it becomes clear that the *Chamberlain (hexagonal packing)* model predicts the best value for the transverse linear thermal expansion coefficient compared with the experimental value. The *Chamberlain (hexagonal packing)* model slightly over estimates the value, while the *Chamberlain (square packing)* model underestimates the experimental value. The other models, *CCA*, *Chamis*, *Schneider*, *Rule of Mixtures* and *Shapery* increasingly overestimate the experimental value for the composite transverse linear thermal expansion coefficient.

4 Conclusions

After verifying the predicted properties with the measured properties of the composite material, the following can be concluded.

1. All properties, elastic and thermal, in the fibre direction are predicted exactly the same with all models. The prediction is a slight overestimation of the experimental value.
2. The elastic properties, transverse to the fibre direction, are predicted best with the *CCA* model. The model slightly overestimates the experimental value.
3. The in-plane elastic properties, in-plane shear modulus and Poisson constant, are predicted most accurate using the *CCA* model. The model again slightly overestimates the properties with respect to the experimental value.
4. The transverse linear thermal expansion coefficient is best predicted with the Chamberlain hexagonal model. The model slightly overestimates the experimental value.

5 List of symbols

Symbol	Description
V_f	overall fibre volume fraction
$V_{f\,max}$	maximum fibre volume fraction
V_m	matrix volume fraction
E_{cL}	longitudinal composite modulus
E_{cT}	transverse composite modulus
G_{cLT}	in-plane composite shear modulus
G_{cTT}	transverse composite shear modulus
ν_{cLT}	in-plane composite Poisson ratio
ν_{cTT}	transverse composite Poisson ratio
α_{cL}	longitudinal composite linear thermal expansion coefficient
α_{cT}	transverse composite linear thermal expansion coefficient
E_f	fibre modulus
G_f	fibre shear modulus
ν_f	fibre Poisson ratio
E_{fL}	longitudinal fibre modulus
E_{fT}	transverse fibre modulus
G_{fLT}	in-plane fibre shear modulus
G_{fTT}	transverse fibre shear modulus
ν_{fLT}	in-plane fibre Poisson ratio
ν_{fTT}	transverse fibre Poisson ratio
α_f	fibre linear thermal expansion coefficient
α_{fL}	longitudinal fibre linear thermal expansion coefficient
α_{fT}	transverse fibre linear thermal expansion coefficient
E_m	matrix modulus
G_m	matrix shear modulus
ν_m	matrix Poisson ratio
E_{mL}	longitudinal matrix modulus
E_{mT}	transverse matrix modulus
G_{mLT}	in-plane matrix shear modulus
G_{mTT}	transverse matrix shear modulus
ν_{mLT}	in-plane matrix Poisson ratio
ν_{mTT}	transverse matrix Poisson ratio
α_m	matrix linear thermal expansion coefficient
α_{mL}	longitudinal matrix linear thermal expansion coefficient
α_{mT}	transverse matrix linear thermal expansion coefficient

6 References

1. McCullough R.L., *Micromechanical Materials Modelling*, Delaware composites and design encyclopædia, Technomic, Basel, 1991.

2. Chawla K.K., *Material Research and Engineering*, Composite Materials, Science and Enginering, Springer Verlag, , Berlin, 1987.

3. Hashin Z., *Theory of reinforced materials*, CR-1974, NASA.

4. Hashin Z., *Analyses of composite materials*, Journal of applied mechanics, 50:481.

5. Chamis C.C., *NASA Tech. Memo 8320*, 1983

6. Whitney J.M., *Micromechanical Materials Modelling*, Delaware composites and design encyclopædia, Technomic, Basel, 1991.

7. Nijhof A.H.J., *Ontwerpen in vezelversterkte kunststoffen*, TU Delft, 1990.

8. Shapery R.A., *Thermal Expansion Coefficients of Composite Materials Based on Energy Principles*, Journal of Composite Materials, 2:380, 1968.

9. Schneider W., *Wärmeausdehnungskoeffizienten und Wärmespannungen von Glassfaser/Kuststoff-Verbunden*, Kunststoffe, Bd.63, pp.992, 1973.

10. Chamberlain N.J., *BAC Rep. No. SON (P) 33*, 1968.

11. Rogers K.F.. Phillips L.N., Kingston-Lee D.M., Yates B., Overy M.J., Sargent J.P. & McCalla B.A., *The thermal expansion of carbon fibre-reinforced plastics*, Journal of materials science 12, pp.718-734, 1977.

12. Bunsell A.R., *Fibre Reinforcements for Composite Materials*, Composite Materials Series 2, Elsevier, 1994.

13. Peters S.T., *Handbook of Composites*, Second Edition, Chapman & Hall, 1997.

14. Ishai O., *Engineering mechanics of composite Materials*, Oxford University Press, 1994.

15. Lamers E.A.D., C++ class Micromechanical, University of Twente, 1999.